Karlsruhe Institute of Technology

ETP-KA/2022-04

Simulation-based Sensitivity Study of short-lived Axion-Like Particles in B Meson Decays at the Belle II Experiment

Lucas Weidemann

Masterthesis

28th March 2022

Institute of Experimental Particle Physics (ETP)

Advisor: Prof. Dr. Torben Ferber
Coadvisor: Prof. Dr. Markus Klute

Editing time: 28th March 2021 – 28th March 2022

Karlsruhe Institute of Technology

ETP-KA/2022-04

Simulationsbasierte Sensitivitätsstudie von kurzlebigen Axion-ähnlichen Teilchen in B-Meson-Zerfällen am Belle II Experiment

Lucas Weidemann

Masterarbeit

28. März 2022

Institut für Experimentelle Teilchenphysik (ETP)

Referent:	Prof. Dr. Torben Ferber
Korreferent:	Prof. Dr. Markus Klute

Bearbeitungszeit: 28. März 2021 – 28. März 2022

Ich versichere wahrheitsgemäß, die Arbeit selbstständig angefertigt, alle benutzten Hilfsmittel vollständig und genau angegeben und alles kenntlich gemacht zu haben, was aus Arbeiten anderer unverändert oder mit Abänderungen entnommen wurde.

Karlsruhe, 28. März 2022

. . . . . .

(**Lucas Weidemann**)

Disclaimer

The simulation-based sensitivity study of short-lived axion-like particles in $B^{\pm} \to K^{\pm}a$ decays presented in this thesis was proposed to me by Dr. Torben Ferber and Dr. Pablo Goldenzweig. The analysis outline was designed by them and me. I performed the entirety of the analysis as presented in this thesis, with exception of the selection validation of the signal-side reconstruction (section 4.1.1) and the summary of the systematic uncertainties (section 5.4). The former was studied by Alexander Heidelbach, and for the latter I was advised by Dr. Goldenzweig. The software framework for the simulation of the events, the detector simulation and the event reconstruction was provided by the Belle II Collaboration. The signal MC was produced by me, the background MC by the Belle II Collaboration. All results are worded by me. All figures were created by me, unless otherwise stated.

Contents

1. Introduction

"The plain boring stuff that, by default, we expect to be true." These are the words Grégory Schott uses in [1] to describe the Standard Model of particle physics (SM) when searching for new physics. The Standard Model is one of the best models for describing our universe and provides comprehensive insights into elementary particles and their mutual interactions. However, there are some phenomena for which it provides no explanation. These are, for example, dark matter or dark mediators that interact with Standard Model and dark matter particles [2]. To describe such phenomena, new theories are added to the Standard Model. These theories are tested in collider experiments, which provide the perfect environment to search for new physics. For this purpose, it is necessary to prove that a measurement is not exclusively a result of known SM processes, but that new physics processes have additionally contributed to it.

One of the best-motivated extensions to the SM are so-called axion-like particles (ALPs). They arise as pseudo Nambu-Goldstone bosons from a spontaneously broken U(1) symmetry and dominantly interact with SM gauge bosons [3]. They are being searched for at the Belle II experiment in Japan. There, at the SuperKEKB accelerator, electrons and positrons collide with a center-of-mass energy of $\sqrt{s} = 10.58\,\mathrm{GeV/c^2}$. This corresponds to the energy needed to produce the $\Upsilon(4S)$ resonance. This decays almost exclusively into a B meson pair, whose decay products are subsequently recorded by the Belle II detector [4, 5].

The decay studied in this analysis is $B^{\pm} \to K^{\pm}a(\to \gamma\gamma)$. It is of interest because a virtual W boson is produced during this process that emits the ALP. This allows measuring the coupling of the ALP to the W boson. Until recently, this decay was rather poorly studied experimentally [6]. Subsequently, the ALP decays instantaneously into two photons. Since the mass of the ALP m_a is unknown, the challenge in such a search is to perform an analysis for each ALP mass hypothesis to which the Belle II experiment is sensitive.

The objective of this thesis is to determine the expected sensitivity of the branching fraction $\mathcal{B}(B^{\pm} \to K^{\pm}a(\to \gamma\gamma))$ for each of these ALP mass hypotheses. In chapter 2 a more detailed motivation for searching for axion-like particles and some important theoretical foundations are presented. An overview of the Belle II experiment and the analyzed data samples are provided in chapter 3. Chapter 4 focuses on the optimization of the event selection for all ALP mass hypotheses. This is followed by the signal extraction and determination of the expected sensitivity in chapter 5. A summary of the analysis and possible next steps are presented in chapter 6.

2. Motivation and Theoretical Foundations

This chapter provides some physical motivations for the search for axion-like particles in B meson decays. A historical review of the axion is presented in section 2.1. It is explained what motivates the introduction of the axion and some important characteristics are summarized. The relationship between the axion and the axion-like particle (ALP) is discussed in section 2.2. Also, some phenomena that could be explained by the existence of ALPs are presented. Subsequently, section 2.3 discusses the studied $B^{\pm} \to K^{\pm}a(\to \gamma\gamma)$ process and some aspects of the sensitivity-based search strategy. Finally, section 2.4 presents the most recent results of the BaBar collaboration on this process. Based on this, the objective of this analysis is defined.

2.1. Axions

The axion was postulated 1977/78 by papers of Peccei and Quinn [7, 8], Weinberg [9], and Wilczek [10] to solve the so-called strong CP problem. It arises from the CP violating term in the Lagrangian of quantum chromodynamics (QCD)

$$\mathcal{L}_{\theta_{\mathrm{QCD}}} = -\theta_{\mathrm{QCD}} \frac{\alpha_S}{8\pi} \mathrm{Tr}\Big(G_{\mu\nu}\tilde{G}^{\mu\nu}\Big). \tag{2.1}$$

Here, α_S is the effective QCD coupling, $G_{\mu\nu}$ is the gluon field strength tensor, and $\tilde{G}^{\mu\nu} = \epsilon^{\mu\nu\lambda\rho}G_{\lambda\rho}/2$ its dual [5, chapter 91]. θ_{QCD} is interpreted as an angle, whose value is a number between 0 and 2π. Because of the CP violation in the QCD Lagrangian, it would be expected to measure an electric dipole moment for the neutron. However, none was found yet, but only upper limits could be set for it. This results in an upper limit on $\theta_{\mathrm{QCD}} < 10^{-10}$ [11]. The question that arises now is, why θ_{QCD} is that low and tends to be zero. It is reasonable to assume that an unknown physical process leads to the cancellation of the CP violation in QCD.

For this reason, the global Peccei-Quinn $\mathrm{U}(1)_{\mathrm{PQ}}$ symmetry was introduced. This symmetry is spontaneously broken, which is accompanied consequently by the introduction of a new pseudo Nambu-Goldstone boson, the axion. This adds another term to equation (2.1)

$$\mathcal{L}_{\theta_{\mathrm{QCD}}} = \left(\frac{\phi_{\mathrm{a}}}{f_{\mathrm{a}}} - \theta_{\mathrm{QCD}}\right) \frac{\alpha_S}{8\pi} \mathrm{Tr}\Big(G_{\mu\nu}\tilde{G}^{\mu\nu}\Big), \tag{2.2}$$

where ϕ_{a} denotes the axion field and f_{a} the decay constant of the axion. For $\phi_{\mathrm{a}} = \theta_{\mathrm{QCD}} f_{\mathrm{a}}$ equation (2.2) becomes zero and the CP invariance in QCD would be restored.

The mass of the axion

$$m_{\mathrm{a,QCD}} \approx 5.7\mu\mathrm{eV}\left(\frac{10^{12}\,\mathrm{GeV}}{f_{\mathrm{a}}}\right) \tag{2.3}$$

is coupled directly to its decay constant [12]. Furthermore, depending on the specific model, the axion couples predominantly to gauge bosons [13]. However, the coupling to photons plays a special role and is subject of many axion analyses. The axion coupling to two photons is described via

$$\mathcal{L}_{\mathrm{a}\gamma\gamma} = -\frac{g_{\mathrm{a}\gamma\gamma}}{4}\phi_{\mathrm{a}}F_{\mu\nu}\tilde{F}^{\mu\nu} \tag{2.4}$$

and has a decay width of

$$\Gamma_{\mathrm{a}\to\gamma\gamma} = \frac{g_{\mathrm{a}\gamma\gamma}^2 m_{\mathrm{a}}^3}{64\pi}. \tag{2.5}$$

Here, $F_{\mu\nu}$ is the electromagnetic field strength tensor, $\tilde{F}^{\mu\nu}$ its dual, and $g_{\mathrm{a}\gamma\gamma}$ the coupling constant between axion and photon. Like $m_{\mathrm{a,QCD}}$, the coupling constant $g_{\mathrm{a}\gamma\gamma}$ depends on the decay constant f_{a}. Both values are thus determined by knowing f_{a} [5, chapter 91].

2.2. Axion-Like Particles (ALPs)

An extension to the axion theory is the introduction of axion-like particles (ALPs). In contrast to axions, the mass m_{a} and coupling constant $g_{\mathrm{a}\gamma\gamma}$ of the ALP are independent of each other, which allows them to be in a much larger parameter space. All other characteristics are the same for axions and ALPs [2]. However, ALPs may not provide a solution to the strong CP problem anymore [14], although this is why the axion was introduced in the first place.

Nevertheless, there are a variety of models that support the existence of ALPs. At masses below the MeV scale, some phenomena from cosmology and astrophysics could be explained. ALPs serve as potential dark matter candidates, as so-called weakly interacting slim particles (WISPs) [15]. Above the MeV scale, ALPs become interesting for particle physics. It is assumed that ALPs would decay too fast to be dark matter candidates. However, they can act as a bridge (or mediator) between Standard Model (SM) particles and other dark matter particles. They would also provide an explanation for the anomalous magnetic dipole moment of the muon [16].

2.3. The $\mathrm{B}^{\pm} \to \mathrm{K}^{\pm}\mathrm{a}(\to \gamma\gamma)$ Decay

In this analysis, the coupling to the W boson is studied. In contrast to the coupling to gluons and photons, this coupling is less explored. The coupling of the ALP with the W boson is described with

$$\mathcal{L} = -\frac{g_{\mathrm{aWW}}}{4}\phi_{\mathrm{a}}\mathrm{W}_{\mu\nu}^{b}\tilde{\mathrm{W}}^{b\mu\nu}. \tag{2.6}$$

Here, g_{aWW} denotes the coupling constant of the axion to the W boson, $\mathrm{W}_{\mu\nu}^{b}$ is the $\mathrm{SU(2)_W}$ gauge-boson field strength tensor and $\tilde{\mathrm{W}}^{b\mu\nu}$ its dual. A direct connection between the ALP coupling to photons and its coupling to W bosons is obtained via

$$g_{\mathrm{a}\gamma\gamma} = g_{\mathrm{a}\gamma\gamma}\sin^2\theta_W, \tag{2.7}$$

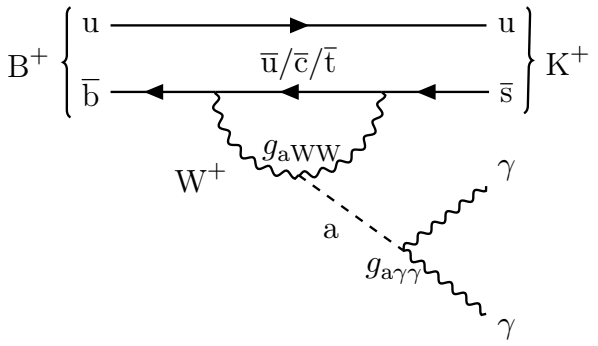

Figure 2.1.: Feynman diagram of the $B^{\pm} \to K^{\pm}a(\to \gamma\gamma)$ decay. The axion-like particle is emitted in an FCNC interaction of the B meson and decays into 2 photons. The process is the same for the charge conjugated decay.

with the Weinberg angle θ_W [6].

Thus, ALPs can be emitted in flavor-changing neutral current (FCNC) interactions, as shown with a Feynman diagram in figure 2.1. The b quark emits a virtual W boson and re-absorbs it, which is accompanied by a double flavor change. This turns the B meson into a kaon. Due to energy and momentum conservation, another particle has to be emitted in this transition [17], such as the ALP. The ALP subsequently decays into two photons. Such FCNC processes are rare, but show a clear signature and are thus well suited for a discovery [3].

In this analysis, it is assumed that the ALP decays instantaneously and only to photons. Since ALPs with masses $m_a \ll m_W$ are studied, this assumption is justified. The ALP mass m_a is determined by using the four-momentum vectors of the photons $\boldsymbol{p}_{\gamma_i}$ and calculating the invariant mass $M_{\gamma\gamma} = \sqrt{\boldsymbol{p}_{\gamma_1}\boldsymbol{p}_{\gamma_2}}/c$. Ideally, $M_{\gamma\gamma}$ should be equal to m_a. So a resonance in the $M_{\gamma\gamma}$ spectrum is sought. It must be considered that there will be other resonances in the $M_{\gamma\gamma}$ spectrum due to π^0, η, and η' decays into two photons [3]. Since it is almost impossible to distinguish peaks of these decays from an ALP peak, the regions around the corresponding peaks will be excluded.

2.4. Results of BaBar

In November 2021, the BaBar Collaboration presented its studies on the $B^{\pm} \to K^{\pm}a(\to \gamma\gamma)$ decay. The search takes place in range $0.175\,\mathrm{GeV/c^2} < m_a < m_{B^{\pm}} - m_{K^{\pm}} \approx 4.78\,\mathrm{GeV/c^2}$. The ranges 0.10 - $0.175\,\mathrm{GeV/c^2}$, 0.45 - $0.63\,\mathrm{GeV/c^2}$, and 0.91 - $1.01\,\mathrm{GeV/c^2}$ are excluded because of the π^0, η, and η' resonances.

Furthermore, the case of long-lived ALPs, which travel up to $c\tau_a = 10\,\mathrm{cm}$ before decaying, was investigated as well. The search was designed for a data set of $4.72 \cdot 10^8$ $B\overline{B}$ meson pairs recorded with the BaBar detector. This corresponds to an integrated luminosity of $424\,\mathrm{fb}^{-1}$.

For details on the exact procedure of the BaBar study, the interested reader is referred to [6]. Their results are shown in figure 2.2 and figure 2.3. BaBar had not found any evidence for

an ALP signal. But they were able to set upper limits of $\sim 10^{-7}$ on the branching fraction of $B^{\pm} \to K^{\pm}a(\to \gamma\gamma)$ and decreased the upper limits on the coupling constant g_{aWW} to $\sim 10^{-5}\,\mathrm{GeV}^{-1}$ (labeled g_{aW} in figure 2.3).

The objective of this study is to determine the expected sensitivity for the branching fraction $B^{\pm} \to K^{\pm}a(\to \gamma\gamma)$ at the Belle II experiment and compare it to that of BaBar. In case of similar or even better performance, there is a good chance to set better upper limits in further studies or maybe even to discover an ALP signal.

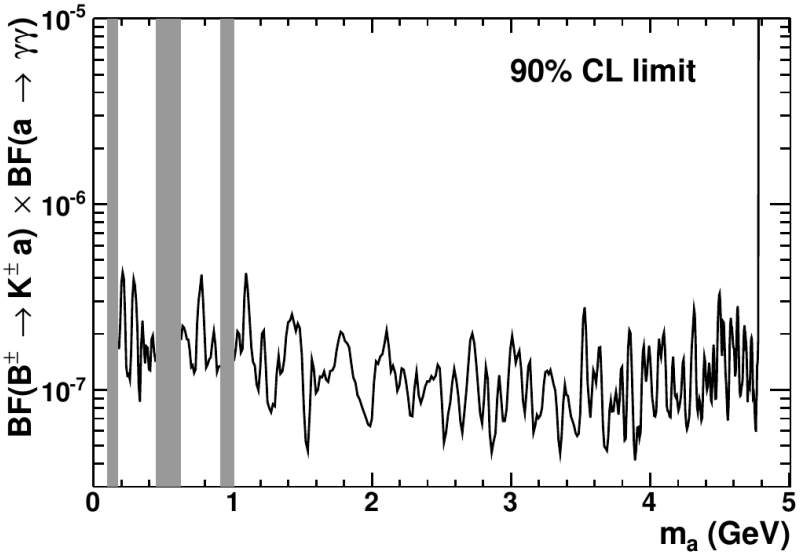

Figure 2.2.: 90 % confidence level (CL) upper limits on the branching fraction $B^{\pm} \to K^{\pm}a$ for promptly decaying ALPs as a function of m_a. The regions around the π^0, η, and η' masses are excluded, which is indicated by the vertical gray bands. Result of the BaBar search for $B^{\pm} \to K^{\pm}a$, taken from [6].

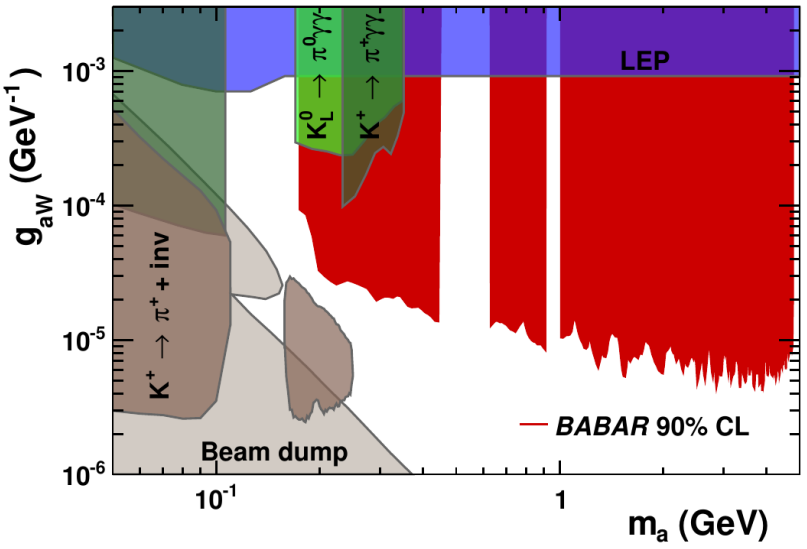

Figure 2.3.: 90 % confidence level (CL) upper limits on the coupling g_{aW} as function of m_a. The BaBar result (red) is displayed with other existing constraints (blue, green, gray, brown). Taken from [6].

3. The Belle II Experiment

The analysis is performed as part of the Belle II experiment, which is presented in more detail in this chapter. Section 3.1 describes the SuperKEKB accelerator used to collide particles for the Belle II experiment. The setup of the Belle II detector is described in section 3.2. Two subdetectors are presented in more detail, because of their importance for this analysis. An essential part of the analysis is performed using the Belle II Analysis Software Framework, which is described in section 3.3. The simulated Monte Carlo (MC) datasets used for the analysis are introduced in section 3.4.

3.1. SuperKEKB

SuperKEKB is a particle accelerator facility in Japan where electrons and positrons collide with center-of-mass energies in the regions of the Υ resonances. It is mainly operated at a center-of-mass energy of $\sqrt{s} = 10.58\,\mathrm{GeV/c^2}$. This corresponds to the $\Upsilon(4S)$ resonance, which decays to $> 96\,\%$ in a B meson pair. The luminosity is ~ 40 times higher than its predecessor KEKB. SuperKEKB aims to deliver an integrated luminosity of $50\,\mathrm{ab}^{-1}$ [18].

A schematic view of the SuperKEKB collider is shown in figure 3.1. It is composed of two storage rings, one for the electrons and one for the positrons. Before being injected, the electrons are pre-accelerated in a linear accelerator (linac). The positrons are produced in a damping ring by shooting electrons at a tungsten plate. They are subsequently injected into their ring. The electrons are accelerated to an energy of $7\,\mathrm{GeV}$ and the positrons to $4\,\mathrm{GeV}$ [4].

One of the main tasks of the Belle II experiment is to measure the CP violation in the electroweak interaction. This is achieved by colliding the electrons and positrons with different energies to obtain a boost in the center-of-mass system. By measuring the distance the B mesons travel before they decay, their lifetime is determined. Due to the collision of elementary particles, the initial state is well known, which allows precise measurements of events where particles such as neutrinos or dark matter leave the detector undetected [18].

3.2. The Belle II Detector

The Belle II detector is an upgraded version of its predecessor Belle. It consists of different subdetector layers to measure the different particles from the collision. A schematic view of the detector is shown in figure 3.2. The innermost part is composed of the Pixel

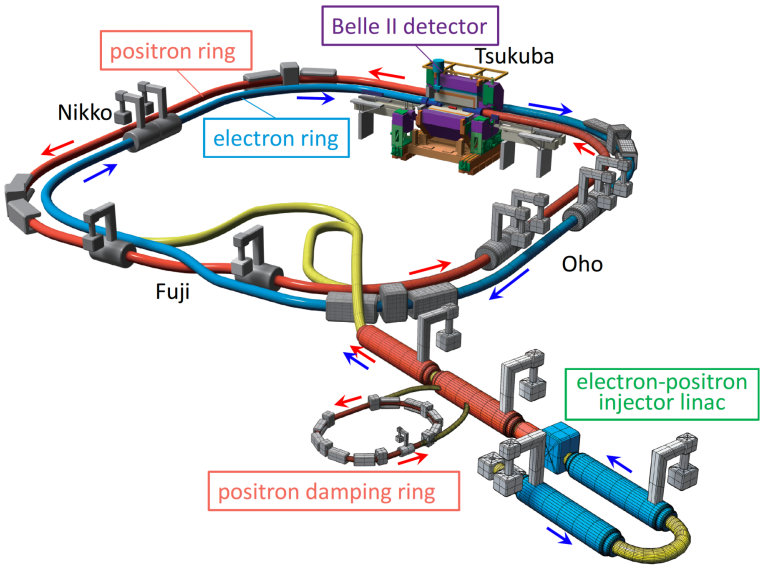

Figure 3.1.: Schematic view of the SuperKEKB collider. The positrons (red) are produced in a damping ring and pre-accelerated along with electrons (blue) by using a linear accelerator (linac). They are directed into their respective storage rings and collided at the Tsukuba straight section, the location of the Belle II experiment. Taken from [4].

Detector (PXD), the Silicon Vertex Detector (SVD), and the Central Drift Chamber (CDC). These three components form the tracking system of the Belle II detector. For particle identification, the Time-Of-Propagation (TOP) counter is used in the barrel region and the Aerogel Ring-Imaging Cherenkov Detector (ARICH) in the forward end-cap region. Around this is the Electromagnetic Calorimeter (ECL), which measures the energy and position of photons and electrons. Outside the ECL is a superconducting solenoid with a magnetic field of 1.5 T, which is used to curve the trajectory of charged particles and allows to measure their momenta. The Belle II detector is completed with the K_L- Muon detector (KLM) as the outermost layer [18, chapter 3].

The relevant subdetectors for this analysis are the CDC and the ECL. Therefore, these are presented in more detail. Further information about all subdetector systems can be found in [18, 19].

Central Drift Chamber (CDC)

The CDC is the central tracking device of the Belle II detector and provides an angular coverage of $17^\circ \leq \theta \leq 150^\circ$. It is filled with a gas mixture and consists of 56 cylindrically arranged layers composed of 8400 drift cells. As the charged particles pass through the CDC, they lose a certain amount of energy $\mathrm{d}E/\mathrm{dx}$ depending on their momentum. This is measured in the drift cells and used for particle localization and identification. By reconstructing the track and measuring its curvature, the particle momentum is determined.

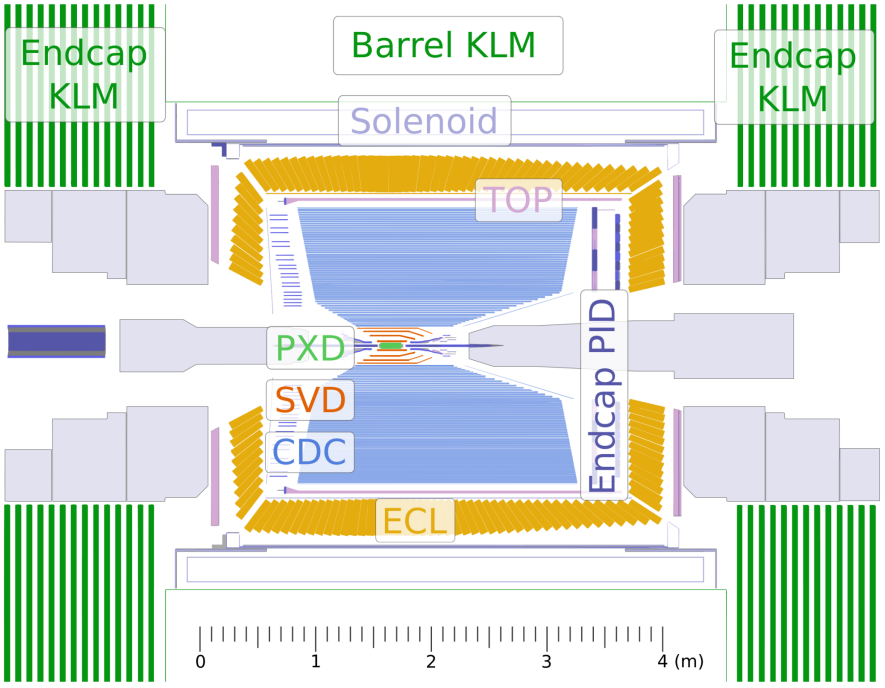

Figure 3.2.: Cross section of the Belle II detector. The ARICH is called Endcap PID in this illustration. Taken from [20].

Electromagnetic Calorimeter (ECL)

The detection of photons, the determination of their energy, and their angular coordinates are some of the main tasks of the ECL. It consists of a total of 8736 thallium-doped caesium iodide CsI(TI) crystals arranged cylindrically in the detector. They do not point directly to the interaction point but are slightly tilted instead. This suppresses photons passing through crystal gaps. When they pass through a crystal, scintillation light is produced, which is measured by photodiodes. As the CDC, the ECL covers a region of $17^\circ \leq \theta \leq 150^\circ$. Other particles interacting with the ECL are electrons, muons, and hadrons.

3.3. Belle II Analysis Software Framework

The amount of data and the complexity of algorithms for processing them are continuously increasing, not only in high-energy physics. A reliable software framework is needed to facilitate the data processing. For Belle II, this is the Belle II Analysis Software Framework (basf2) [21]. A so-called steering file is set up for data processing. It is used to arrange the different basf2 modules, which are mostly written in C++, in a path. Such a path is processed sequentially in a fixed sequence. It is possible to attach conditions to the modules and also to create several paths. In this analysis basf2 is used for

- simulation of $B^{\pm} \to K^{\pm}a(\to \gamma\gamma)$ events,
- detector simulation,

- reconstruction, such as tracking, clustering, and particle identification,
- offline analysis, such as the event reconstruction.

After the offline analysis, the processed data is stored in ROOT [22] files. This allows the data to be analyzed further afterwards.

3.4. Monte Carlo Samples

To study the $B^{\pm} \to K^{\pm}a(\to \gamma\gamma)$ decay, Monte Carlo (MC) samples of the decay are initially analyzed. These are simulated events that should behave as much as possible like events from the real detector. As indicated in the previous section, the events, the detector, and its response to the various particles are simulated for this purpose. The detector is simulated with GEANT4 [23]. Several event generators are available for the simulation of the events.

In contrast to real data from the detector (in the following this is referred to as data), in MC it is well known which particles participated in an event and where they originated from. This allows studying differences between the analyzed events (signal) and other events with similar signatures (background). To avoid personal bias in the analysis, each step is performed, optimized, and verified on MC. Only at the end of an analysis, the result is compared with data from the signal region. The individual MC samples used in this analysis are presented below.

$B^{\pm} \to K^{\pm}a(\to \gamma\gamma)$ signal MC sample

Since the mass of the ALP is unknown, several MC samples have to be generated for the analysis, each with a different ALP mass m_a. The study of the BaBar Collaboration used a mass range of 0.10 -4.78 $\mathrm{GeV/c^2}$, which is adopted in this analysis [6]. A total of 13 signal MC samples are generated with 5000 events each. The EVTGEN [24] package is used for the event simulation. Figure 3.3 shows what such a signal event looks like in the Belle II detector.

$B\overline{B}$ background MC sample (generic)

The $B\overline{B}$ MC sample is also called generic and is provided by the Belle II Collaboration. It contains events of the form $\Upsilon(4S) \to B^+B^-$ and $\Upsilon(4S) \to B^0\overline{B}^0$. The sample size corresponds to an integrated luminosity of 100 $\mathrm{fb^{-1}}$, which are approximately $1.05 \cdot 10^8$ events [25, chapter 3].

$q\bar{q}$ background MC sample (continuum)

The $e^-e^+ \to q\bar{q}$ MC sample is also called continuum and is provided by the Belle II Collaboration. Here events without an $\Upsilon(4S)$ resonance are considered, in which therefore no B mesons but light hadrons are produced with $q \in \{u, d, s, c\}$. Also the continuum sample size corresponds to an integrated luminosity of 100 $\mathrm{fb^{-1}}$, which are approximately $3.75 \cdot 10^8$ events [18, chapter 4].

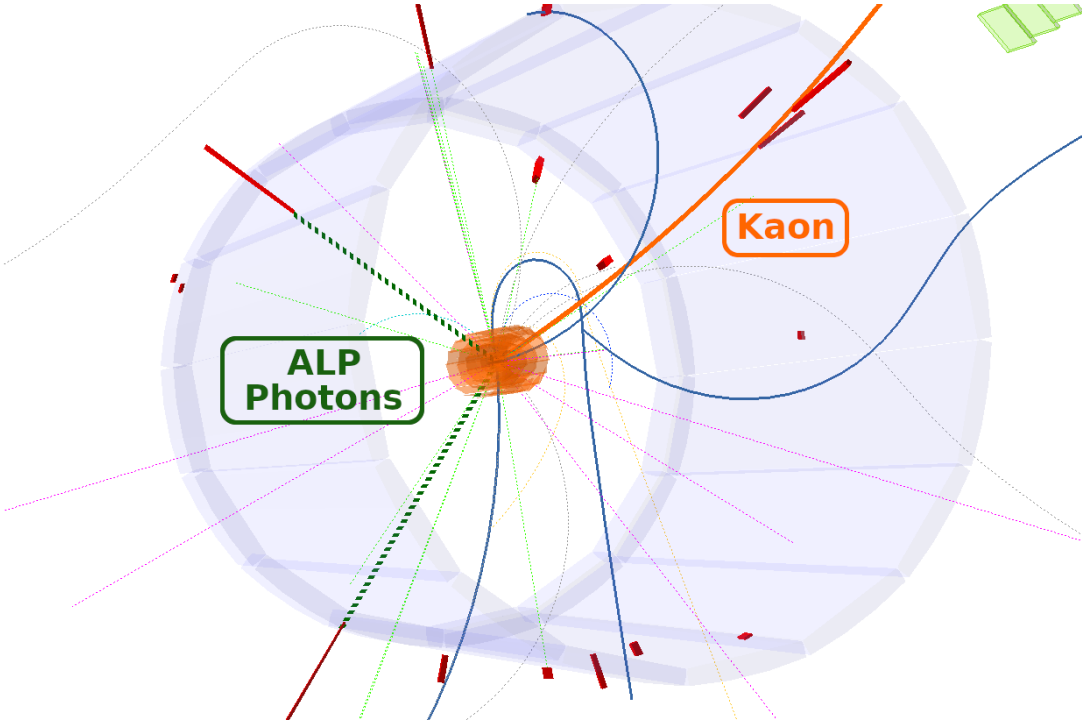

Figure 3.3.: Event display showing a simulated $B^{\pm} \to K^{\pm}a(\to \gamma\gamma)$ event with a $2.0\,\mathrm{GeV/c^2}$ ALP. The photons from the ALP decay (green, dashed) travel straight to the ECL. The kaon (orange, solid) travels in a curved trajectory, leaves a track in the CDC, and passes through the ECL, depositing some of its energy. The remaining lines indicate other particles of the event.

4. Event Selection

An essential part of particle physics analyses is the selection of relevant events including the signal decay out of the enormous number of collision events that occur. Section 4.1 deals with the reconstruction of the simulated $B^{\pm} \to K^{\pm}a$ events. The distribution in which the signal will be extracted is the invariant mass of the two ALP photons $M_{\gamma\gamma}$, which is analyzed in more detail in section 4.2. Section 4.3 focuses on optimizing the separation between signal and background events for different ALP masses. This is also reflected in section 4.4, where the optimized selections are applied to the entire m_a spectrum.

4.1. Event Reconstruction

This section explains the reconstruction of the two photons and the kaon from the $B^{\pm} \to K^{\pm}a(\to \gamma\gamma)$ decay and how these particles are subsequently combined to form a B meson. Furthermore, it is discussed why it is worthwhile to consider particles in the same event which do not belong to the studied decay. It is also shown why - contrary to the search of the BaBar Collaboration [6] - ALPs with a mass of $m_a = 4.78\,\mathrm{GeV/c^2}$ are excluded from this analysis.

4.1.1. Signal-Side Reconstruction

For the photon reconstruction, one looks for a cluster of energy depositions in the ECL with no corresponding track assigned (neutral cluster). Therefore, only ECL clusters in a polar angle $\theta \in [17^\circ, 150^\circ]$ are considered, since tracking information from the CDC is available in this region. However, this selection is not yet sufficient, since for example neutral hadrons also exhibit this signature. That is why another selection on $clusterE1E9 > 0.4$ is applied. This is the ratio of the energy depositions between the central crystal with the highest energy *E1* and the 3×3 crystals *E9* surrounding this central crystal. For photons, this value is usually higher than for hadrons, since most of the photon energy is deposited in the central crystal. Due to inelastic scattering, hadronic showers are more diffuse shaped, resulting in more energy depositions in the surrounding crystals [21, 26].

The time and energy reconstruction of particles at the ECL is performed with a waveform fit [27]. ECL clusters for which this fit failed are removed with $clusterErrorTiming < 10^6$ ns, which is the uncertainty of the cluster timing. To reduce the number of photons coming from other processes, only photons with an energy $E > 0.05\,\mathrm{GeV}$ are selected. Since photons leave no track, only the location of their impact in the ECL is known. Therefore,

for the reconstruction of their four-momentum vectors, it is assumed that they originate from the IP. By adding the four-momentum vectors of both ALP photons, one obtains the four-momentum vector of the ALP.

Initially, all particles that leave a track in the CDC are selected as kaons. This means that all track-related parameters are computed using the kaon hypothesis. In order to filter out tracks from background processes, they must meet a few basic criteria. The number of hits in the CDC must be greater than 20 and a close distance of the track origin to the IP are required. For the latter, only tracks with a transverse distance to the IP $dr < 0.5\,\mathrm{cm}$ and for which the z-component of the point of closest approach to the IP $|dz|$ is smaller than 2.0 cm are selected. The kaon and the ALP are then combined to the initial B meson. To reduce the number of wrongly reconstructed B mesons, the beam constrained mass

$$M_{\mathrm{bc}} = \frac{1}{c^2}\sqrt{E_{\mathrm{beam}}^2 - \boldsymbol{p}_{\mathrm{B}}^2 c^2} \tag{4.1}$$

is introduced, where E_{beam} is half the center-of-mass energy of the beam and $\boldsymbol{p}_{\mathrm{B}}$ is the four-momentum vector of the reconstructed B meson candidate. For correctly reconstructed B mesons, M_{bc} is equal to the B meson mass $m_{\mathrm{B}} = 5.28\,\mathrm{GeV/c^2}$ [5], which leads to a peak in the M_{bc} distribution. For an even better background reduction ΔE is introduced, which is the difference between the energy of the B meson candidate and E_{beam} [21]. The selections on $M_{\mathrm{bc}} > 5.20\,\mathrm{GeV/c^2}$ and $|\Delta E| < 0.3\,\mathrm{GeV}$ were chosen quite loosely in order to find the best selection values in section 4.3 and to check whether they depend on the generated ALP mass m_{a}.

A summary of all selection criteria for reconstructing $\mathrm{B}^{\pm} \to \mathrm{K}^{\pm}\mathrm{a}(\to \gamma\gamma)$ events is shown in table 4.1. It was verified that the signal efficiency does not drop significantly with these selection criteria applied. The signal efficiency is the ratio between the number of correctly reconstructed signal events and the number of generated signal events. It is shown in figure 4.1 for all generated signal MC samples after performing the event reconstruction.

Up to an ALP with mass $m_{\mathrm{a}} = 4.5\,\mathrm{GeV/c^2}$, the signal efficiency is between 47 % and 56 %. For $m_{\mathrm{a}} = 0.1\,\mathrm{GeV/c^2}$ a drop is seen, which is explained by the fact that the ALP gained a high momentum. As a result, both photons from the ALP decay move almost parallel and leave a single cluster in the ECL, which is reconstructed as one photon. A drop is also seen for higher ALP masses, which even decreases to nearly 0 % at $m_{\mathrm{a}} = 4.78\,\mathrm{GeV/c^2}$. The cause and impact of this are discussed in more detail in section 4.1.3.

4.1.2. Rest of Event

After the reconstruction of the signal B meson $\mathrm{B_{sig}}$, it is useful to take a look at the remaining clusters and tracks in an event. They are called rest of event (ROE). If $\mathrm{B_{sig}}$ is correctly reconstructed, all information about its partner B meson $\mathrm{B_{tag}}$ is in the ROE. This information is used in section 4.3 to identify and suppress continuum events. An illustration of both B meson decays is shown in figure 4.2.

Besides the partner B meson the ROE contains also other particles, like δ-rays or beam background particles, which are not created in the $\mathrm{e^+e^-}$ collision [21]. To remove such particles, some selections are applied to all particles in the ROE. For continuum suppression,

Table 4.1.: Overview of the selections for reconstructing the decay $B^{\pm} \to K^{\pm}a(\to \gamma\gamma)$.

Particle	Variable	Selection
γ	$clusterE1E9$	< 0.4
	$clusterErrorTiming$	$< 10^6$ ns
	E	> 0.05 GeV
	θ	$\in [17^\circ, 150^\circ]$
$K^{\pm}$	$clusterNHits$	> 20
	dr	< 0.5 cm
	$\lvert dz \rvert$	< 2.0 cm
	θ	$\in [17^\circ, 150^\circ]$
$B^{\pm}$	M_{bc}	$> 5.20\,\mathrm{GeV/c^2}$
	$\lvert \Delta E \rvert$	< 0.3 GeV

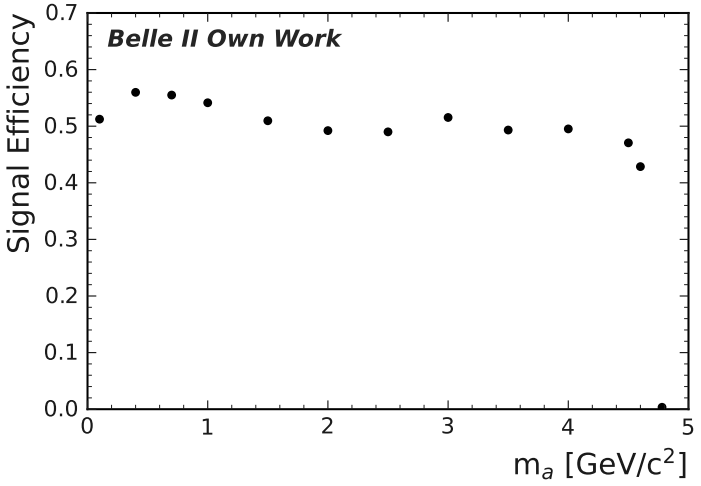

Figure 4.1.: Signal efficiencies of the simulated $B^{\pm} \to K^{\pm}a(\to \gamma\gamma)$ samples after performing the signal-side reconstruction.

only particles in the ROE with a momentum of 3.2 GeV/c or less in the CMS frame are selected. Additionally, a charged particle must leave at least one hit in the CDC or the measured momentum of a particle must be 0.05 GeV/c or greater to be selected. A summary of all mentioned criteria is listed in table 4.2.

Table 4.2.: Overview of the selection criteria for calculating the continuum suppression variables in section 4.3. A particle only needs to satisfy the condition for the momentum p or the number of hits in the CDC in order to be selected.

Variable	Selection
p_{CMS}	$\leq 3.2\,\mathrm{GeV/c}$
p	$\geq 0.05\,\mathrm{GeV/c}$
$nCDCHits$	> 0

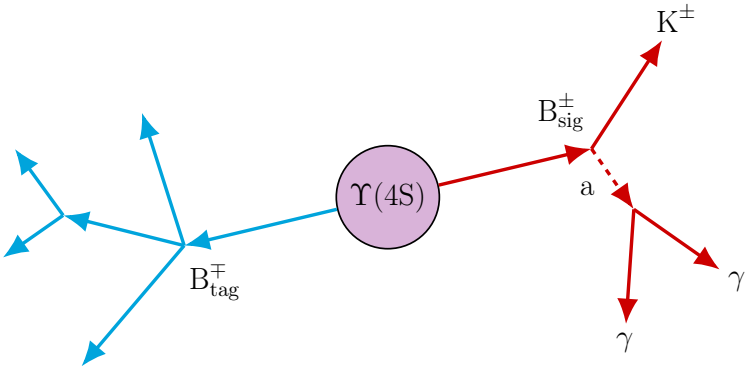

Figure 4.2.: Illustration of an $\Upsilon(4S)$ event containing the decay $B^{\pm} \to K^{\pm}a(\to \gamma\gamma)$ (red). The short dashed line at the ALP indicates its instantaneous decay. The second B meson B_{tag} (blue) decays randomly into different particles.

4.1.3. Choice of Upper m_a Value

As stated in section 3.4, the simulation-based sensitivity study is performed in the region $m_{\mathrm{a}} \in [0.10, 4.78]\,\mathrm{GeV/c^2}$. However, the reconstruction of the signal B meson fails for heavy ALPs with $m_{\mathrm{a}} = 4.78\,\mathrm{GeV/c^2}$, because the maximum kaon momentum is

$$p_{\mathrm{K},CMS} = (m_{\Upsilon(4S)} - m_{\mathrm{K}} - m_{\mathrm{a}}) \cdot c \approx 0.10\,\mathrm{GeV/c} \tag{4.2}$$

in the CMS frame. For kaons with such small momentum, it is very difficult to reach the outer detector layers. This effect is also observed in [28, chapter 3]. Charged particles with a transverse momentum $p_T < 0.3\,\mathrm{GeV/c}$ can curl within the CDC. As a result, only a few events are reconstructed correctly. This is shown on the left plot of figure 4.3. On the right plot, it is seen that for ALPs with $m_{\mathrm{a}} = 4.60\,\mathrm{GeV/c^2}$ the number of correctly reconstructed events increases significantly and is therefore set as the upper mass limit in this analysis.

4.2. Fit Variable $M_{\gamma\gamma}$

The ALP signal is performed in the invariant diphoton mass distribution $M_{\gamma\gamma}$ where an ALP signal appears as a narrow peak. Its shape follows a double-sided crystal ball function which is defined as

$$f(x;\mu,\sigma,\alpha_l,n_l,\alpha_r,n_r) = \begin{cases} A_l \cdot (B_l - \frac{x-\mu}{\sigma})^{-n_l}, & \text{for } \frac{x-\mu}{\sigma} < -\alpha_l \\ \exp\left(-\frac{(x-\mu)^2}{2\sigma^2}\right), & \text{for } -\alpha_l \leq \frac{x-\mu}{\sigma} \leq \alpha_r \\ A_r \cdot (B_r - \frac{x-\mu}{\sigma})^{-n_r}, & \text{for } \frac{x-\mu}{\sigma} > \alpha_r \end{cases} \tag{4.3}$$

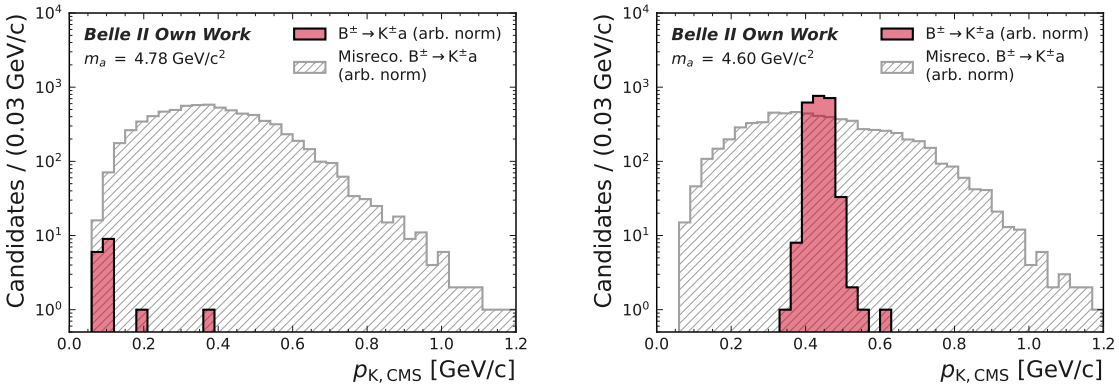

(a) $m_a = 4.78\,\mathrm{GeV/c^2}$. (b) $m_a = 4.60\,\mathrm{GeV/c^2}$.

Figure 4.3.: Distribution of the kaon momentum in the CMS frame $p_{K,CMS}$ for simulated $B^\pm \to K^\pm a(\to \gamma\gamma)$ events. The distributions for correctly reconstructed (red) and misreconstructed (gray) signal candidates are shown. For $m_a = 4.78\,\mathrm{GeV/c^2}$ the kaon momentum is too small to reconstruct the entire event. For $m_a = 4.60\,\mathrm{GeV/c^2}$ the number of correctly reconstructed events already increases significantly. For visualization purposes, only the variable range from 0.0 to 1.2 is shown.

with

$$A_{l/r} = \left(\frac{n_{l/r}}{\alpha_{l/r}}\right)^{n_{l/r}} \cdot \exp\left(-\frac{\alpha_{l/r}^2}{2}\right), \quad B_{l/r} = \frac{n_{l/r}}{\alpha_{l/r}} - \alpha_{l/r}. \tag{4.4}$$

It is composed of a Gaussian core and two power law tails on the left and right side. The number of events under the pdf is extracted by extending the pdf with a yield [29].

To study one particular ALP mass hypothesis, it is important for the event selection to retain as much signal and as little background events as possible at the corresponding location in the $M_{\gamma\gamma}$ spectrum. Therefore, for the optimization of the event selection in section 4.3, only candidates around the ALP peak are considered. Afterwards, this selection is relaxed to better model the underlying background distribution with more statistics.

For a better resolution of the peak and for reducing the number of background events below, a mass constrained fit is performed on $M_{\gamma\gamma}$. In this process, it is required, that the four-momentum vectors of the photon, kaon, and B meson candidates are consistent with their nominal mass. For this purpose, the TreeFitter module of basf2 is used [30]. The effect of this method is seen in figure 4.4, where the $M_{\gamma\gamma}$ distribution of the correctly reconstructed events with (red) and without (blue) a mass constrained fit is plotted. It is easy to see that with greater mass, the effect of the mass constrained fit becomes greater too. The $M_{\gamma\gamma}$ range for the event selection optimization in section 4.3 is determined by using the maximum likelihood method to fit the double-sided crystal ball function over the signal events. The definition of the maximum likelihood method is given in section 5.1. Based on the fit, the 3 % to 99 % inter-percentile range is calculated. This is the range between the first 3 % of all signal events on the left side and the last 1 % on the right side.

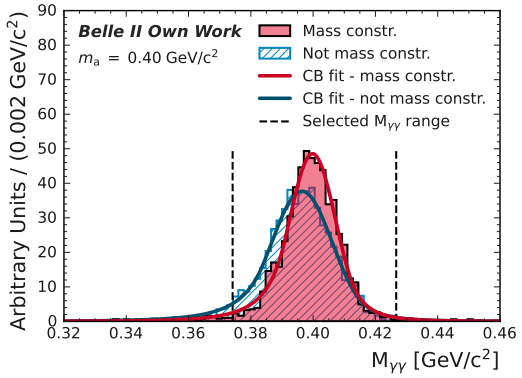

(a) $M_{\gamma\gamma}$ distribution for $m_a = 0.40\,\mathrm{GeV/c^2}$ in range $[0.32, 0.46]\,\mathrm{GeV/c^2}$.

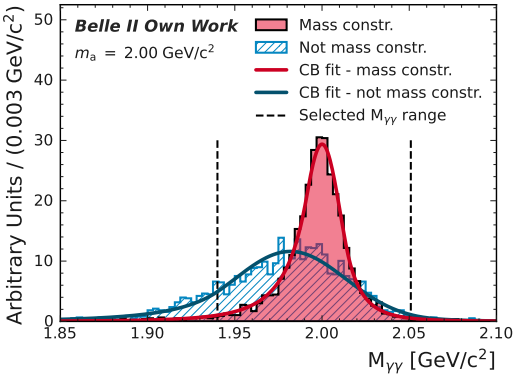

(b) $M_{\gamma\gamma}$ distribution for $m_a = 2.00\,\mathrm{GeV/c^2}$ in range $[1.85, 2.10]\,\mathrm{GeV/c^2}$.

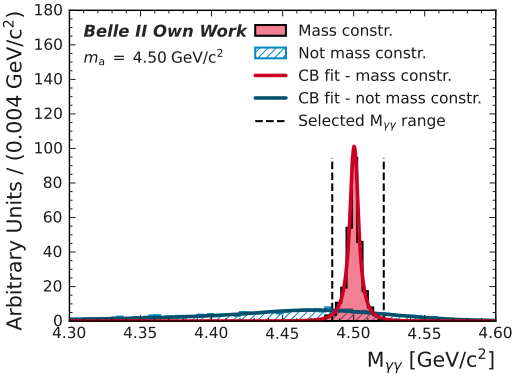

(c) $M_{\gamma\gamma}$ distribution for $m_a = 4.50\,\mathrm{GeV/c^2}$ in range $[4.30, 4.60]\,\mathrm{GeV/c^2}$.

Figure 4.4.: Distribution of $M_{\gamma\gamma}$ with and without using a mass constrained fit for correctly reconstructed signal events. Double-sided crystal ball functions are fitted over both distributions. The $M_{\gamma\gamma}$ range is selected by calculating the 3 % to 99 % inter-percentile range from the fit, which is indicated by the two black dashed lines. To see the different effects of the mass constrained fit, distributions of three different ALP masses are shown.

4.3. Punzi Optimization

As mentioned in the previous chapters, events with other decays than $B^{\pm} \to K^{\pm}a$ are wrongly selected. They are distinguished by analyzing different event properties, which are presented in section 4.3.1. In section 4.3.2 the so-called Punzi figure of merit is introduced, which is used to evaluate the event selection for different m_a. It is subsequently used in section 4.3.3 to optimize the selections from section 4.3.1. The concept of this optimization is presented in detail as well.

4.3.1. Background Suppressing Variables

After performing the event reconstruction in section 4.1, one has to deal with a large number of background events in addition to the correctly reconstructed signal events. This

is simply because random particles are generated that mimic the signature of a signal event. Fortunately, there are other characteristics in which they are distinguishable.

A description of these characteristics is given by different variables, which are presented next. The extent to which these variables perform an event classification is discussed and whether a general selection for all m_{a} is reasonable. For this, plots are shown for each variable after performing the event reconstruction in section 4.1. To analyze differences for ALPs with different m_{a}, the distributions for ALPs with $0.4\,\mathrm{GeV/c^2}$, $2.0\,\mathrm{GeV/c^2}$, and $4.5\,\mathrm{GeV/c^2}$ are shown. Only candidates within the $M_{\gamma\gamma}$ window from section 4.2 are displayed. For comparison, the same histograms after applying the final event selection in section 4.4 are presented. Only the selection of the plotted variable is not applied.

M_{bc} and ΔE

Early studies of the selection optimization in section 4.3.3 showed an optimal selection on $M_{\mathrm{bc}} > 5.27\,\mathrm{GeV/c^2}$ which does not change for different m_{a}. The optimal selection on ΔE on the other hand shows a dependence on m_{a} and is therefore analyzed in more detail in the next subsections. Plots for M_{bc} are displayed in figure 4.6 and for ΔE in figure 4.7.

π^0 Mass Veto

One of the main sources for photons in an event originates from π^0 decays. For this reason, a so-called π^0 mass veto is introduced. A signal photon γ_{sig} is combined with a photon in the ROE, for which the invariant mass $M_{\gamma_{\mathrm{sig}}\gamma_{\mathrm{ROE}}}$ is closest to the π^0 mass $m_{\pi^0} = 0.135\,\mathrm{GeV/c^2}$ [5].

At first only candidates for which $M_{\gamma_{\mathrm{sig}}\gamma_{\mathrm{ROE}}} \in [0.08, 0.20]\,\mathrm{GeV/c^2}$ are selected. This is displayed in figure 4.8. Note that candidates that do not fulfill the mentioned criterion are not visible in these plots. Their shapes are very similar and a clear peak around m_{π^0} is seen for all of them, which originates dominantly from continuum events. Therefore a general selection of $M_{\gamma_{\mathrm{sig}}\gamma_{\mathrm{ROE}}} \notin [0.11, 0.15]\,\mathrm{GeV/c^2}$ is applied, independent of m_{a}.

Binary Likelihood Ratio $\mathcal{R}_{K^\pm/\pi^\pm}$

Up until now, the only condition for selecting a kaon candidate was a clear track in the CDC. This means that initially every tracked charged particle will be classified as a kaon. For particle identification at the Belle II experiment, the information from each subdetector is combined to compute a likelihood for each charged particle hypothesis. Since pions are the largest source for background events in this analysis, the binary likelihood ratio

$$\mathcal{R}_{K^\pm/\pi^\pm} = \frac{\mathcal{L}_{K^\pm}}{\mathcal{L}_{K^\pm} + \mathcal{L}_{\pi^\pm}} \tag{4.5}$$

is introduced to deal specifically with the separation of kaons and pions. Similar to M_{bc}, the optimal selection is uncorrelated to m_{a} and is very loose with $\mathcal{R}_{K^\pm/\pi^\pm} > 0.02$. This is shown in figure 4.9.

Energy of lower-energy Photon E_{γ_l}

The two photons produced in the ALP decay normally have different amounts of energy. A useful separation for signal and background events is provided by E_{γ_l}, which is the energy of the lower-energy photon. The energy of the photons strongly depends on m_a and the selection for all m_a is therefore optimized in the upcoming subsections. Plots for this are displayed in figure 4.10.

Continuum Variables R_2 and $|\cos\theta_T|$

The explanations in this section are based on chapter 5 of [31], where more information about background suppression for B decays can be found.

Because of their large quantity, there are still a significant amount of continuum events, even after including the previously stated selections. The notable difference in the event topology between continuum and $\mathrm{B\overline{B}}$ events, as displayed in figure 4.5, is exploited. Only a fraction of the beam energy is used to produce the light $q\bar{q}$ hadrons. The rest remains as kinetic energy, resulting in the formation of strongly collimated jets. In contrast, the entire energy at the $\Upsilon(4\mathrm{S})$ resonance is used for the $\mathrm{B\overline{B}}$ pair production. The decay products from such events are uniformly distributed.

One of the variables that are used to separate such events is

$$R_2 = \frac{H_2}{H_0} \ , \ \text{with} \ H_k = \sum_{i,j} |\vec{p}_i||\vec{p}_j| P_k(\cos\theta_{i,j}) \ , \tag{4.6}$$

which is the ratio of the second and the zeroth Fox-Wolfram moment. P_k denotes the k-th Legendre polynomial, $\vec{p}_i$ the particle momenta and $\theta_{i,j}$ the angle between them. For two highly collimated jets, R_2 approaches 1 and 0 otherwise, ensuring a good separation. Plots showing the R_2 distributions of different ALP masses are displayed in figure 4.11. The distributions are very similar. But a closer look reveals a slight change in the signal distribution.

Another useful variable is $|\cos\theta_\mathrm{T}|$, where the index T refers to the thrust axis $\vec{T}$. This is a unit vector, for which the total projection of the particle momenta $\vec{p}_i$ is maximized. The angle θ_T is defined as the angle between the thrust axis of the particles from the signal B meson decay and the thrust axis of the particles in the ROE. For continuum events the thrust axis points in the direction of the jets, which move away from each other in opposite directions. Therefore, $|\cos\theta_\mathrm{T}|$ takes values close to 1. In contrast, due to the isotropic distribution of particles from $\mathrm{B\overline{B}}$ events, their thrust axis is randomly distributed. This results in a uniform distribution between $[0, 1]$, making $|\cos\theta_\mathrm{T}|$ a good separating variable between these two types of events. This is observable in figure 4.12.

Between different ALP masses, no difference is recognizable in the distributions on the left. Therefore, one could assume that a general selection for all ALP masses would be sufficient. However, as visible on the right, there are differences in the separation power of the other variables for different m_a. This leaves sometimes more and sometimes fewer background candidates. Therefore, this selection is left floating to avoid removing more signal events than necessary.

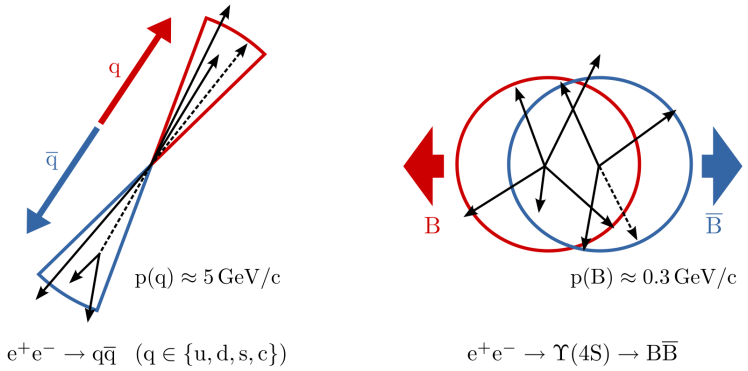

Figure 4.5.: Event shape of a continuum (left) and $B\overline{B}$ (right) event. Due to the higher available momentum, the structure of a continuum event is more jet-like, while $B\overline{B}$ events are more uniformly distributed. Taken from [32].

4.3.2. Punzi Figure of Merit

Despite all these previously introduced criteria, a perfect classification of signal and background events is not possible. The signal and background distributions overlap so that a selection for background rejection is normally always accompanied by the loss of signal events. The question is how many signal events one is willing to sacrifice in order to reject a certain number of background events in return. However, in dark sector searches the cross section for the studied signal and therefore the number of expected signal events are unknown. In such cases, it is quite common to use the Punzi figure of merit (Punzi FOM) [33], which is defined as

$$\text{Punzi FOM} = \frac{\epsilon_{\text{sig}}}{\sigma/2 + \sqrt{N_{\text{bkg}}}}. \tag{4.7}$$

Here, ϵ_{sig} denotes the signal efficiency, which is the number of selected and correctly reconstructed events divided by the number of generated signal events. σ specifies the desired significance, which is $\sigma = 5$ in this analysis, and N_{bkg} is the number of background events. The goal is to find the best selections for each variable that maximizes the Punzi FOM.

A first approach for achieving this goal was a sequential optimization algorithm. The first step is to analyze which of the variables from the previous subsection had the greatest effect on the Punzi FOM and to perform the corresponding selection. This is then repeated sequentially for all variables. However, it turns out that there are a series of problems associated with this approach. For example, the order in which the selections are executed is different for different ALP masses. Another major problem is that some of the variables are highly correlated, such as R_2 and $|\cos\theta_T|$. The selection for one variable changes the optimal selection for the other one and vice versa. Furthermore, the preferred behavior of the Punzi FOM is to perform very tight selections on the first 2-3 variables; the remaining ones only serve for fine-tuning. This would lead to problems if there is a disagreement between MC and data for these specific variables.

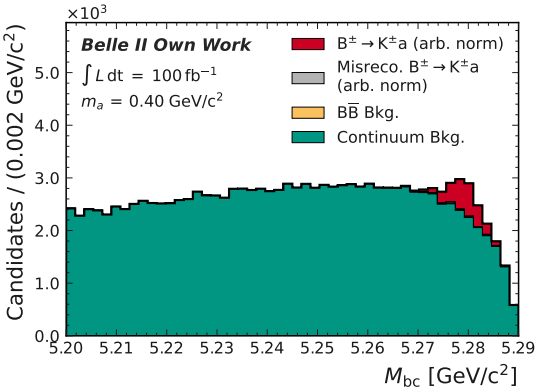

(a) Loose selection. $m_{\text{a}} = 0.40\,\text{GeV}/\text{c}^2$.

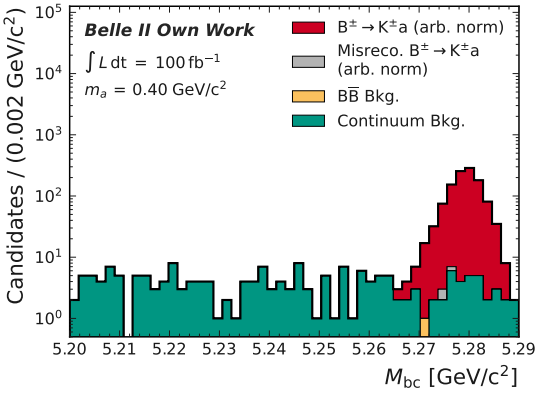

(b) Final selection. $m_{\text{a}} = 0.40\,\text{GeV}/\text{c}^2$.

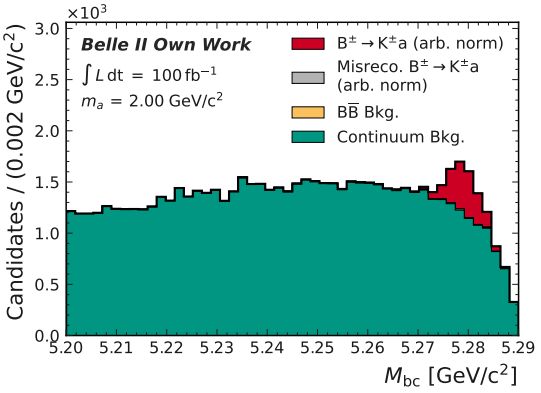

(c) Loose selection. $m_{\text{a}} = 2.00\,\text{GeV}/\text{c}^2$.

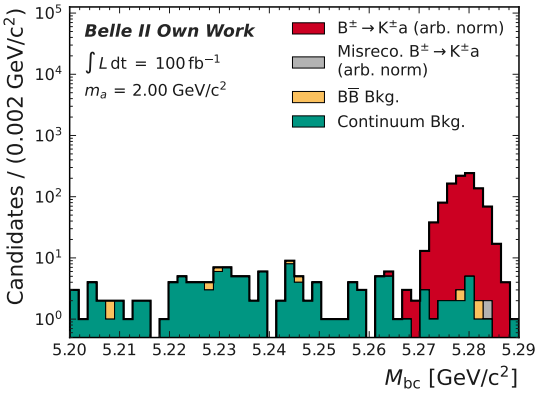

(d) Final selection. $m_{\text{a}} = 2.00\,\text{GeV}/\text{c}^2$.

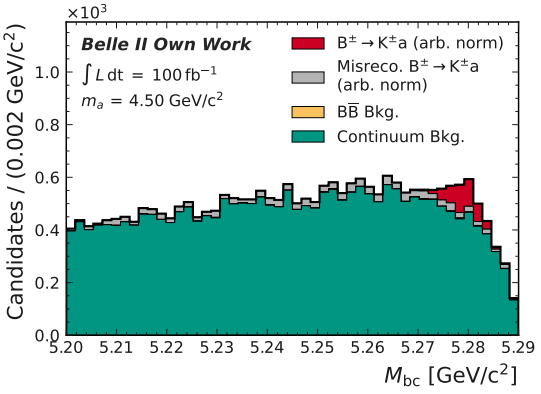

(e) Loose selection. $m_{\text{a}} = 4.50\,\text{GeV}/\text{c}^2$.

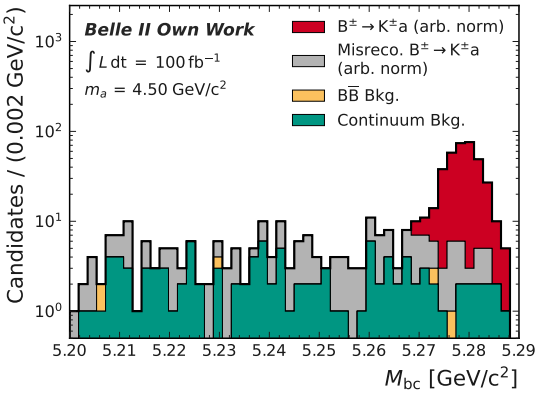

(f) Final selection. $m_{\text{a}} = 4.50\,\text{GeV}/\text{c}^2$.

Figure 4.6.: M_{bc} distributions of simulated signal and background events for three different m_{a} in range $[5.20, 5.29]\,\text{GeV}/\text{c}^2$. All candidates are displayed. On the left: After performing the event reconstruction in section 4.1. On the right: After performing the final event selection in section 4.4. All selections are applied except for the displayed variable.

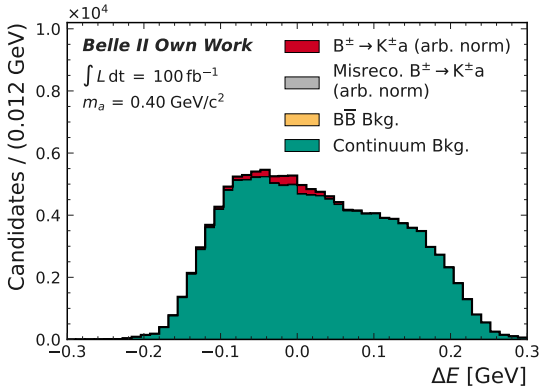

(a) Loose selection. $m_{\mathrm{a}} = 0.40\,\mathrm{GeV/c^2}$.

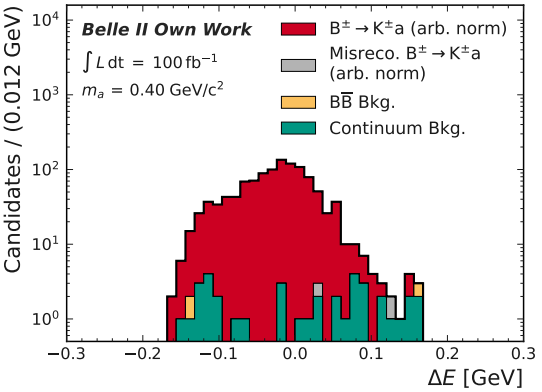

(b) Final selection. $m_{\mathrm{a}} = 0.40\,\mathrm{GeV/c^2}$.

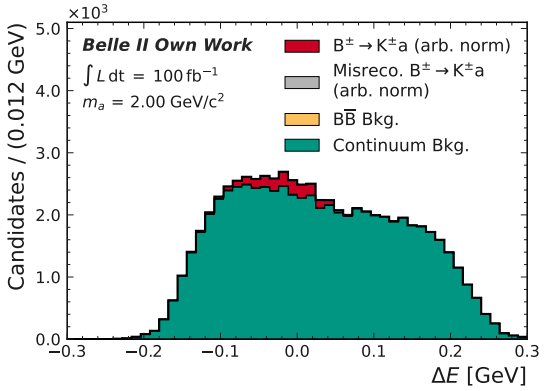

(c) Loose selection. $m_{\mathrm{a}} = 2.00\,\mathrm{GeV/c^2}$.

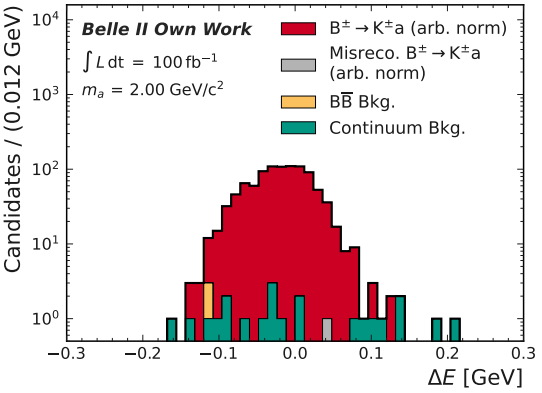

(d) Final selection. $m_{\mathrm{a}} = 2.00\,\mathrm{GeV/c^2}$.

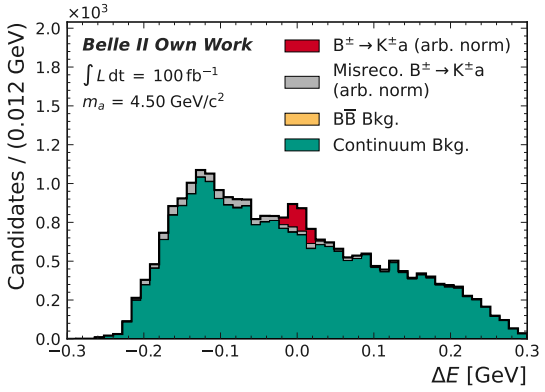

(e) Loose selection. $m_{\mathrm{a}} = 4.50\,\mathrm{GeV/c^2}$.

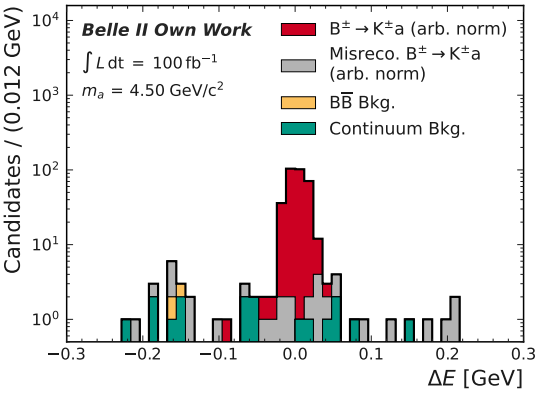

(f) Final selection. $m_{\mathrm{a}} = 4.50\,\mathrm{GeV/c^2}$.

Figure 4.7.: ΔE distributions of simulated signal and background events for three different m_{a} in range $[-0.3, 0.3]\,\mathrm{GeV}$. All candidates are displayed. On the left: After performing the event reconstruction in section 4.1. On the right: After performing the final event selection in section 4.4. All selections are applied except for the plotted variable.

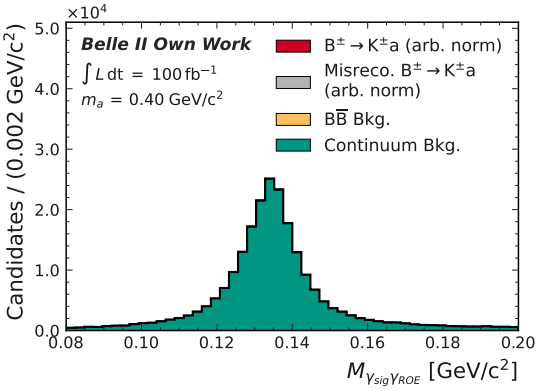

(a) Loose selection. $m_{\mathrm{a}} = 0.40\,\mathrm{GeV/c^2}$.

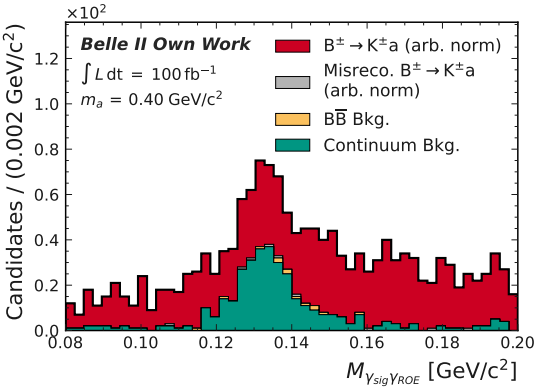

(b) Final selection. $m_{\mathrm{a}} = 0.40\,\mathrm{GeV/c^2}$.

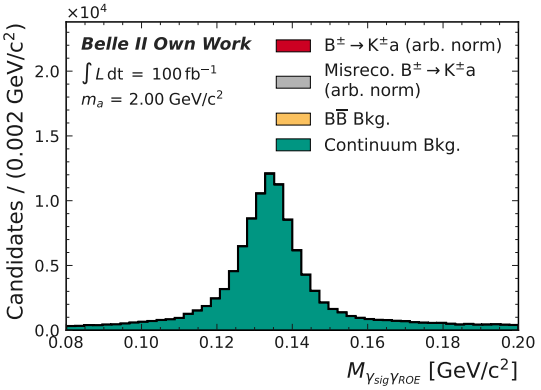

(c) Loose selection. $m_{\mathrm{a}} = 2.00\,\mathrm{GeV/c^2}$.

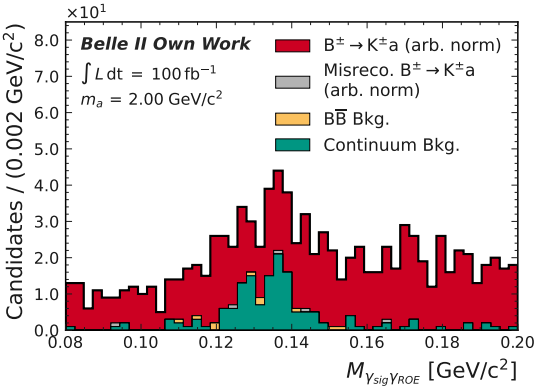

(d) Final selection. $m_{\mathrm{a}} = 2.00\,\mathrm{GeV/c^2}$.

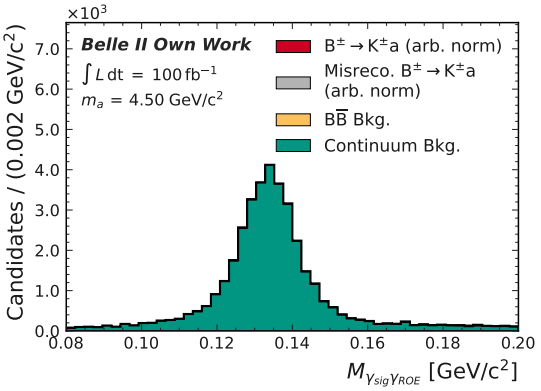

(e) Loose selection. $m_{\mathrm{a}} = 4.50\,\mathrm{GeV/c^2}$.

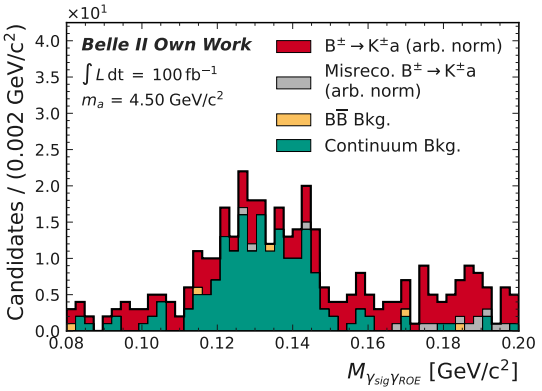

(f) Final selection. $m_{\mathrm{a}} = 4.50\,\mathrm{GeV/c^2}$.

Figure 4.8.: $M_{\gamma_{\mathrm{sig}}\gamma_{\mathrm{ROE}}}$ distributions of simulated signal and background events for three different m_{a} in range $[0.08, 0.20]\,\mathrm{GeV/c^2}$. All candidates are displayed. On the left: After performing the event reconstruction in section 4.1. On the right: After performing the final event selection in section 4.4. All selections are applied except for the plotted variable.

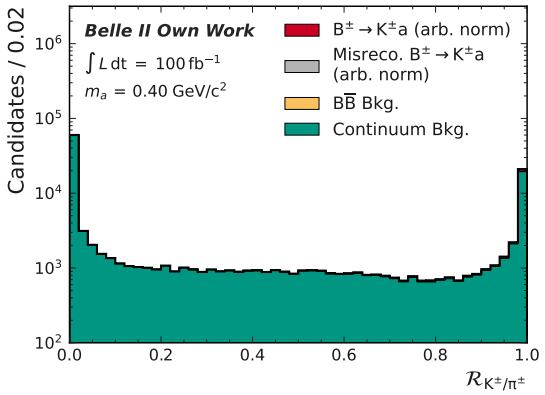

(a) Loose selection. $m_{\mathrm{a}} = 0.40\,\mathrm{GeV/c^2}$.

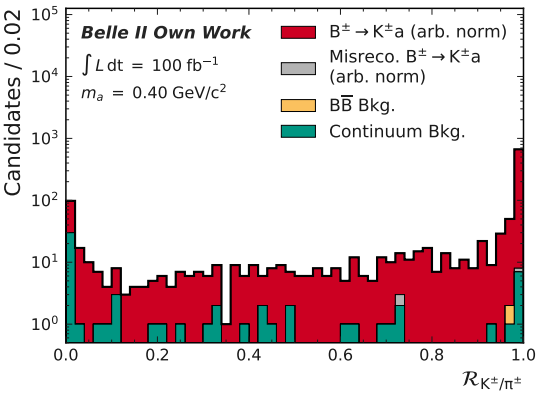

(b) Final selection. $m_{\mathrm{a}} = 0.40\,\mathrm{GeV/c^2}$.

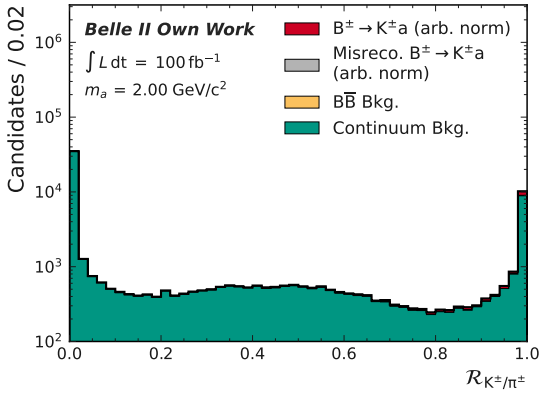

(c) Loose selection. $m_{\mathrm{a}} = 2.00\,\mathrm{GeV/c^2}$.

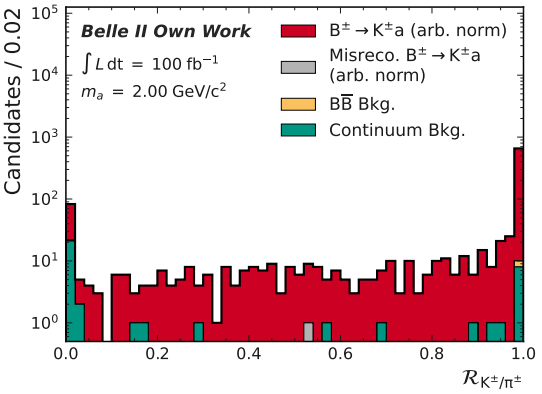

(d) Final selection. $m_{\mathrm{a}} = 2.00\,\mathrm{GeV/c^2}$.

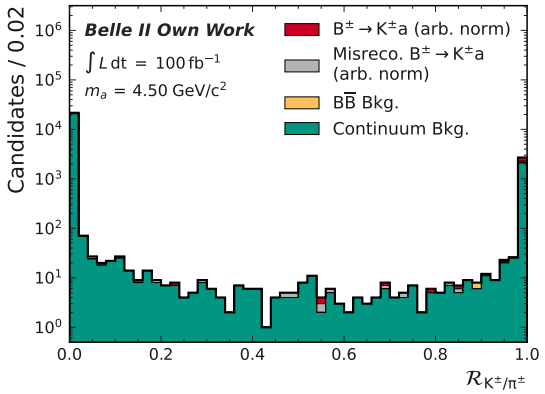

(e) Loose selection. $m_{\mathrm{a}} = 4.50\,\mathrm{GeV/c^2}$.

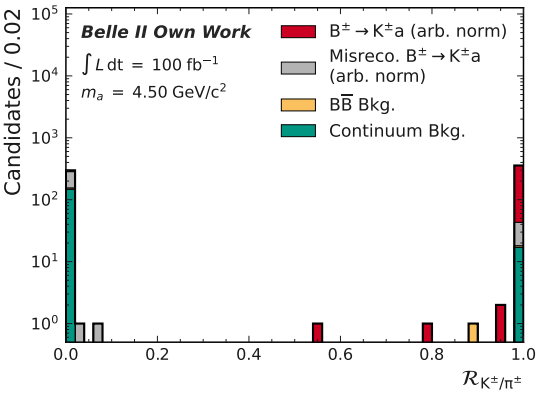

(f) Final selection. $m_{\mathrm{a}} = 4.50\,\mathrm{GeV/c^2}$.

Figure 4.9.: $\mathcal{R}(\mathrm{K}^\pm/\pi^\pm)$ distributions of simulated signal and background events for three different m_{a} in range $[0, 1]$. All candidates are displayed. On the left: After performing the event reconstruction in section 4.1. On the right: After performing the final event selection in section 4.4. All selections are applied except for the plotted variable.

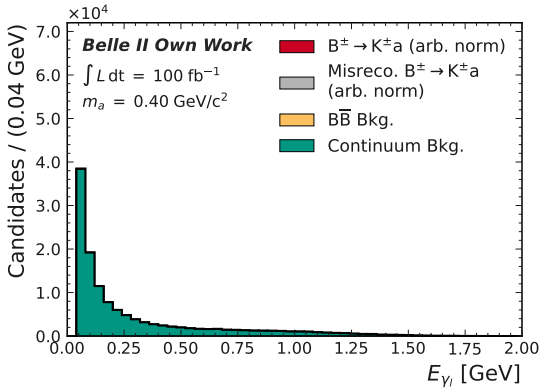

(a) Loose selection. $m_{\mathrm{a}} = 0.40\,\mathrm{GeV/c^2}$. Displayed range: $[0.0, 2.0]\,\mathrm{GeV}$.

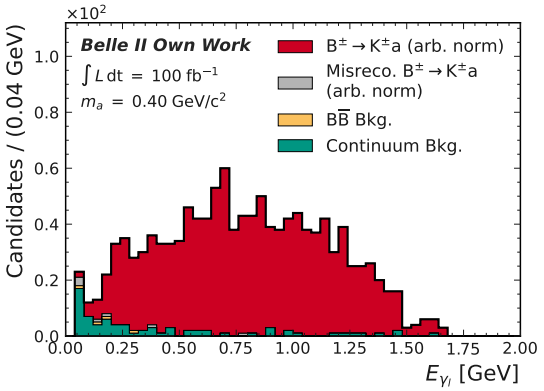

(b) Final selection. $m_{\mathrm{a}} = 0.40\,\mathrm{GeV/c^2}$. Displayed range: $[0.0, 2.0]\,\mathrm{GeV}$.

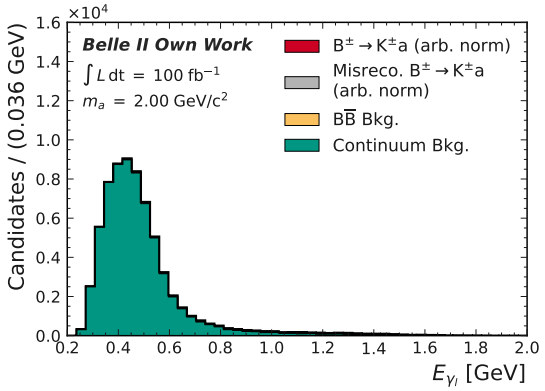

(c) Loose selection. $m_{\mathrm{a}} = 2.00\,\mathrm{GeV/c^2}$. Displayed range: $[0.2, 2.0]\,\mathrm{GeV}$.

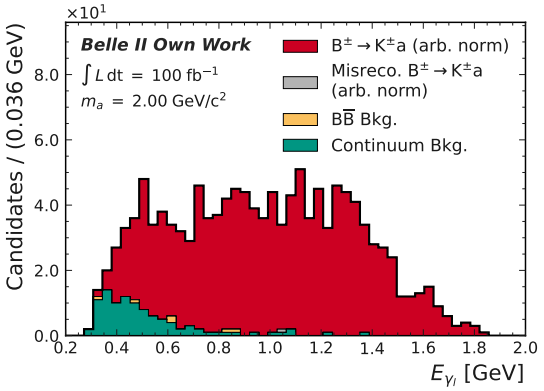

(d) Final selection. $m_{\mathrm{a}} = 2.00\,\mathrm{GeV/c^2}$. Displayed range: $[0.2, 2.0]\,\mathrm{GeV}$.

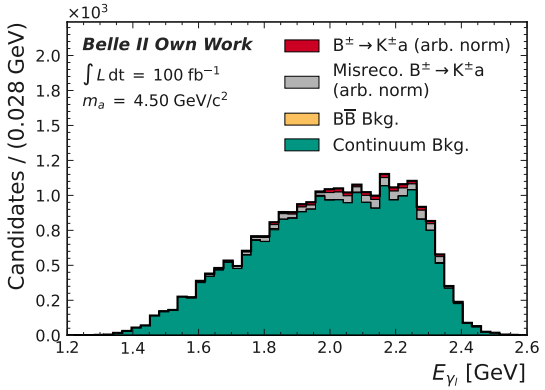

(e) Loose selection. $m_{\mathrm{a}} = 4.50\,\mathrm{GeV/c^2}$. Displayed range: $[1.2, 2.6]\,\mathrm{GeV}$.

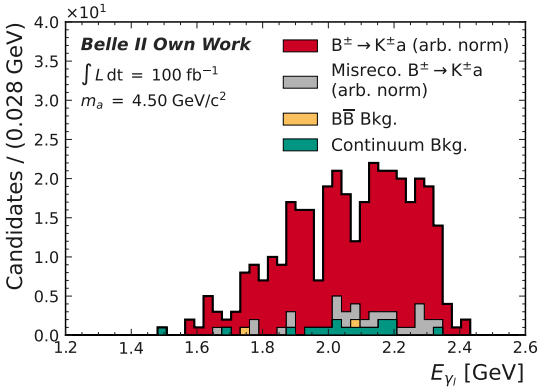

(f) Final selection. $m_{\mathrm{a}} = 4.50\,\mathrm{GeV/c^2}$. Displayed range: $[1.2, 2.6]\,\mathrm{GeV}$.

Figure 4.10.: E_{γ_l} distributions of simulated signal and background events for three different m_{a}. All candidates are displayed. On the left: After performing the event reconstruction in section 4.1. On the right: After performing the final event selection in section 4.4. All selections are applied except for the plotted variable.

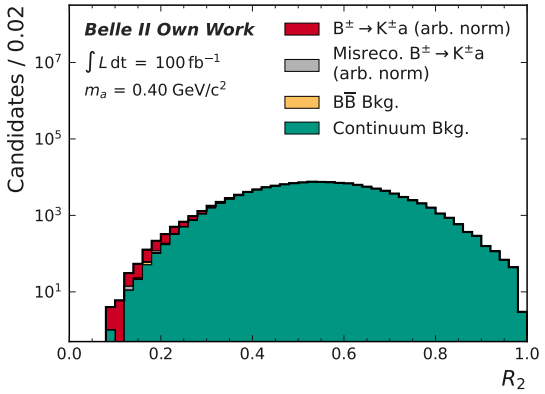

(a) Loose selection. $m_{\mathrm{a}} = 0.40\,\mathrm{GeV/c^2}$.

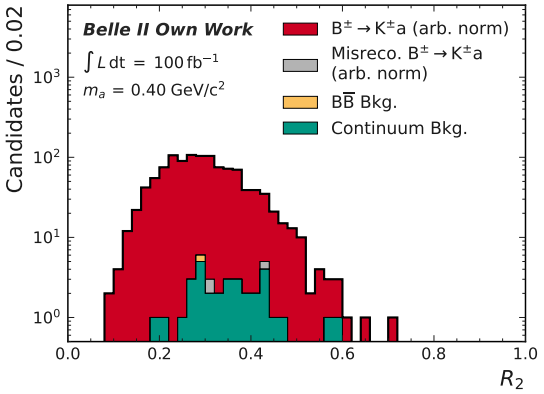

(b) Final selection. $m_{\mathrm{a}} = 0.40\,\mathrm{GeV/c^2}$.

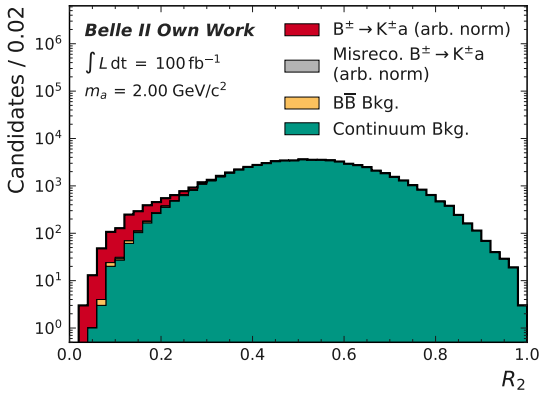

(c) Loose selection. $m_{\mathrm{a}} = 2.00\,\mathrm{GeV/c^2}$.

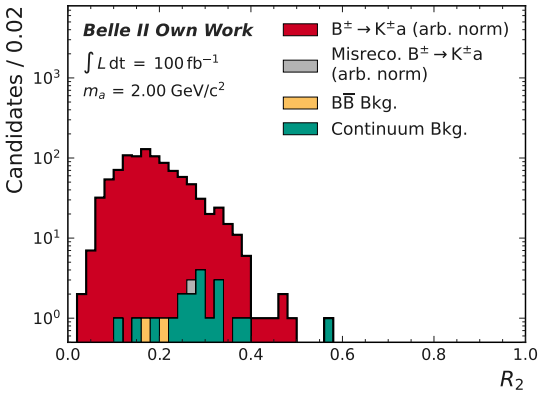

(d) Final selection. $m_{\mathrm{a}} = 2.00\,\mathrm{GeV/c^2}$.

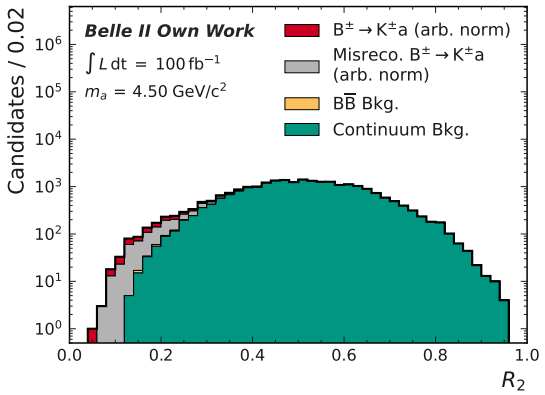

(e) Loose selection. $m_{\mathrm{a}} = 4.50\,\mathrm{GeV/c^2}$.

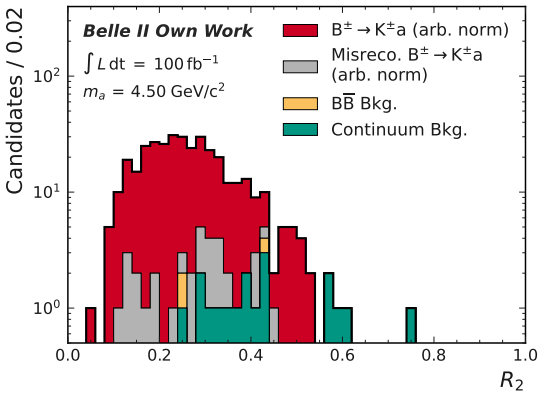

(f) Final selection. $m_{\mathrm{a}} = 4.50\,\mathrm{GeV/c^2}$.

Figure 4.11.: R_2 distributions of simulated signal and background events for three different m_{a} in range $[0, 1]$. All candidates are displayed. On the left: After performing the event reconstruction in section 4.1. On the right: After performing the final event selection in section 4.4. All selections are applied except for the plotted variable.

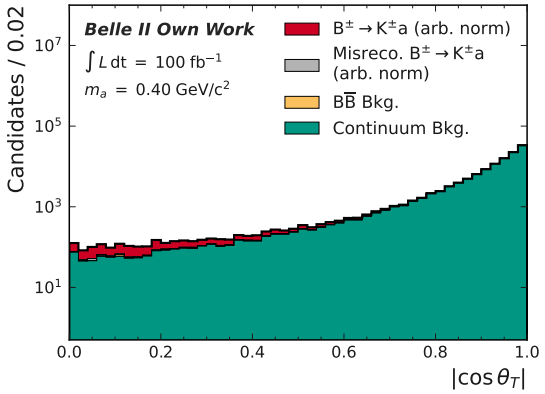

(a) Loose selection. $m_{\mathrm{a}} = 0.40\,\mathrm{GeV/c^2}$.

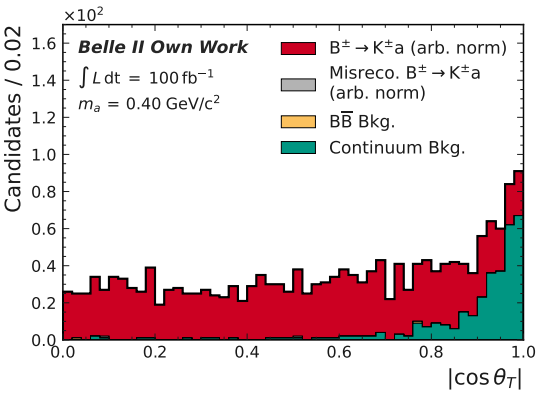

(b) Final selection. $m_{\mathrm{a}} = 0.40\,\mathrm{GeV/c^2}$.

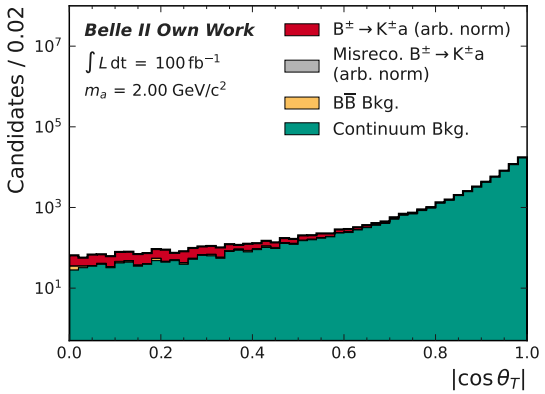

(c) Loose selection. $m_{\mathrm{a}} = 2.00\,\mathrm{GeV/c^2}$.

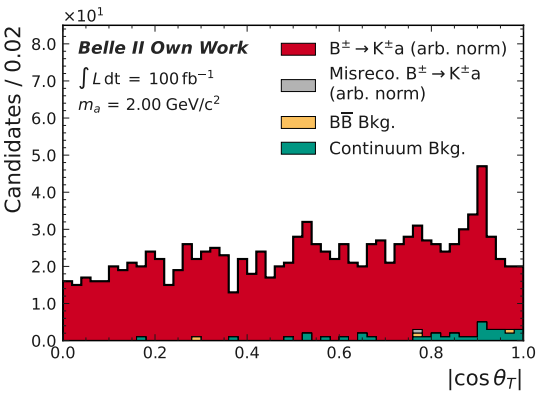

(d) Final selection. $m_{\mathrm{a}} = 2.00\,\mathrm{GeV/c^2}$.

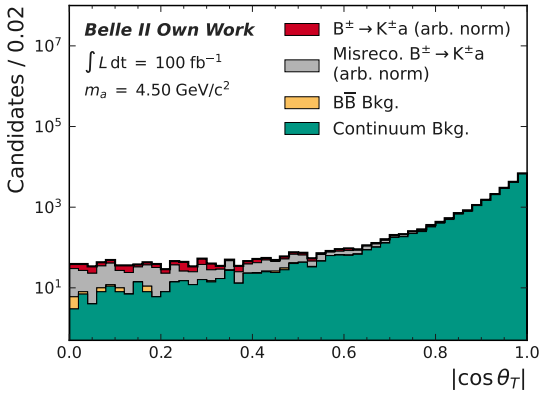

(e) Loose selection.$m_{\mathrm{a}} = 4.50\,\mathrm{GeV/c^2}$.

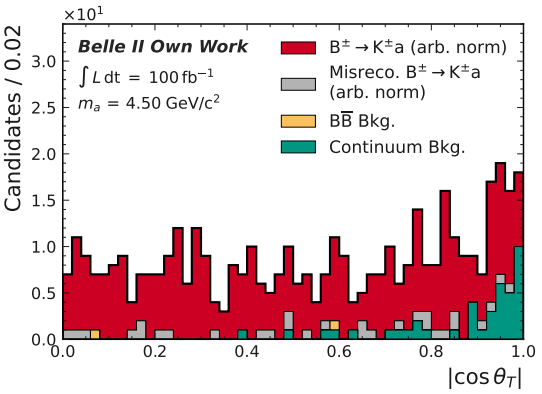

(f) Final selection. $m_{\mathrm{a}} = 4.50\,\mathrm{GeV/c^2}$.

Figure 4.12.: $|\cos\theta_T|$ distributions of simulated signal and background events for three different m_{a} in range $[0, 1]$. All candidates are displayed. On the left: After performing the event reconstruction in section 4.1. On the right: After performing the final event selection in section 4.4. All selections are applied except for the plotted variable.

4.3.3. Punzi Optimization Algorithm

To solve all the problems associated with the first approach, another method was developed to find the maximum of the Punzi FOM. The underlying idea behind it is quite simple and is to include all variables at any time instead of sequentially finding the best selection for each variable. A flow chart showing the sequence of this optimization method is shown in figure 4.13.

First, the $M_{\gamma\gamma}$ selection from section 4.2 is applied to all signal and background candidates. Subsequently, a loose selection is applied to the first variable and determined by how much this selection increases the Punzi FOM. The selection is undone and the previous step is repeated for the second variable. After this process is repeated for all variables, the selection that had the greatest effect on the Punzi FOM is applied permanently to all candidates and the whole process starts again at the first variable. With each iteration, the selections on the individual variables become tighter until finally no selection increases the Punzi FOM anymore. The algorithm is stopped and the optimized selections for a maximal Punzi FOM are returned. Since for some ALP masses the number of background events dropped to zero during the optimization, it was decided to stop it early if the number of background events drops below 20. It is also possible to continue the optimization and perform a zero background analysis. Due to the high additional effort involved in ensuring that there are also zero background events in data, a zero background analysis is not pursued in this study.

To check the performance of the optimization, the Punzi FOM, the signal efficiency, and the number of background events as a function of the chosen selection for each variable are analyzed. All variables are fixed to their optimized values except for the analyzed one. Such plots for ALPs with mass $m_{\mathrm{a}} = 2.0\,\mathrm{GeV/c^2}$ are displayed in figure 4.14. Here, E_{γ_l} provides the greatest separation between signal and background events for this ALP mass. The optimization stopped early due to the small number of background events. More of such control plots for different ALP masses are displayed in appendix A.

4.4. Final Event Selection

The simulation-based sensitivity study is extended by also investigating ALP masses for which no MC samples are generated. The MC samples serve as guidelines to interpolate the selections and signal efficiencies for the masses in between. To be able to perform this interpolation, the behavior of the Punzi optimized selection values has to be adjusted to be robust against outliers. Currently, the selection values jump between different m_{a}, sometimes stronger and sometimes weaker due to a small number of outlying events. To ensure that this does not affect the interpolation, the individual variable distributions for the corresponding ALPs are inspected after applying all other selections and are readjusted by hand. It is checked simultaneously that this readjustment does not have a major impact on the signal efficiency. Chebyshev polynomials were used for the interpolation. The result is shown in figure 4.15.

The selections of the different variables are plotted as a function of m_{a}. The ALP mass $m_{\mathrm{a}} = 0.1\,\mathrm{GeV/c^2}$ was excluded from the interpolation. The reason for that is seen in figure 4.16, where the signal efficiency and the number of background events after applying all selections are plotted as function of m_{a}. For $m_{\mathrm{a}} = 0.1\,\mathrm{GeV/c^2}$ the number of background

events highly increases while the signal efficiency is the lowest. Further investigations show that this is due to a large number of photons coming from π^0 decays still appearing in the region around $M_{\gamma\gamma} = 0.1\,\mathrm{GeV/c^2}$. Therefore, this mass region is removed not only from the interpolation but also from this analysis (see section 5.3). The situation for ALPs with $m_\mathrm{a} = 1.0\,\mathrm{GeV/c^2}$ is similar. Here, the background is higher due to photons coming from η' decays. However, with similar signal efficiency as for the neighboring m_a, the number of background events is still manageable. Therefore, this ALP mass is not excluded.

To interpolate the signal efficiencies in figure 4.16 Chebyshev polynomials are used again. The signal efficiencies are obtained by fitting the corresponding $M_{\gamma\gamma}$ distribution of the signal events after applying all selections. The signal yield is extracted from the fit and divided by the number of generated signal events. The fit uncertainty on the signal yield is used as uncertainty on the signal efficiency. Furthermore, a pull plot is shown below, which indicates how well the interpolation describes the data points. The pull is calculated as the difference between the data point and the value of the interpolation at the same position, divided by the uncertainty on the data point.

Up until now, one candidate was always selected randomly per event. Another possibility is trying to select the most likely signal (or best) candidate. To check if a better signal efficiency is achieved with it, the number of candidates per event is counted and the average (multiplicity) for each m_a is calculated. The corresponding selections for each m_a are applied. This is also done for the different types of background events. The result is shown in figure 4.17. The multiplicity for most ALPs is one and only slightly higher for the other ones. This means that an event mostly has only one possible candidate. For heavy ALPs, this is slightly increased due to the rather loose selections. The multiplicity plays a negligible role in this analysis. Therefore, no best candidate selection is performed, but the candidate is selected randomly.

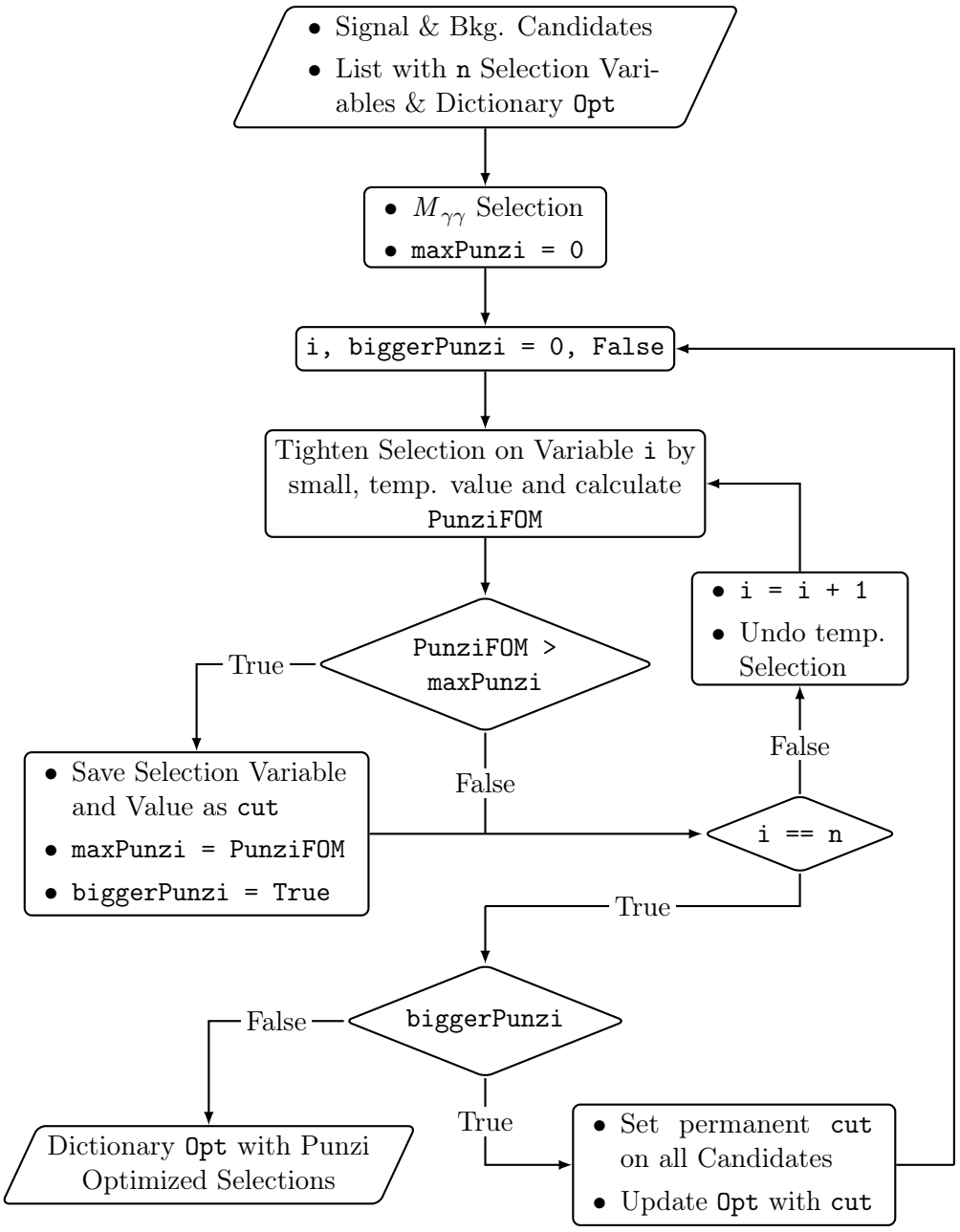

Figure 4.13.: Flow chart with an overview of the Punzi optimization algorithm. One after the other a loose selection is applied on each variable and checked which one maximizes the Punzi FOM. The candidates are filtered according to the selection and the process is repeated for all variables, with the selections getting tighter with each iteration until no further selection provides a larger Punzi FOM. As a result, a dictionary with all Punzi-optimized selections is returned.

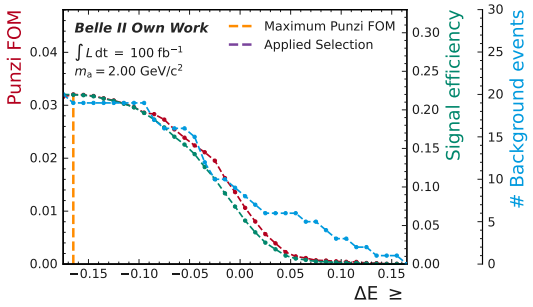

(a) Lower bound on ΔE.

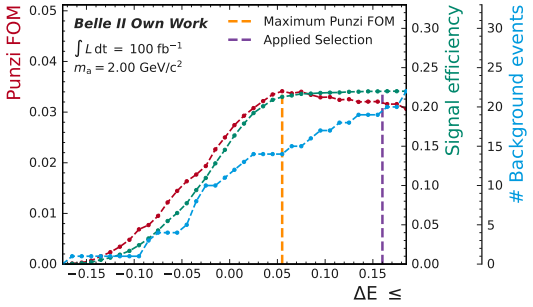

(b) Upper bound on ΔE.

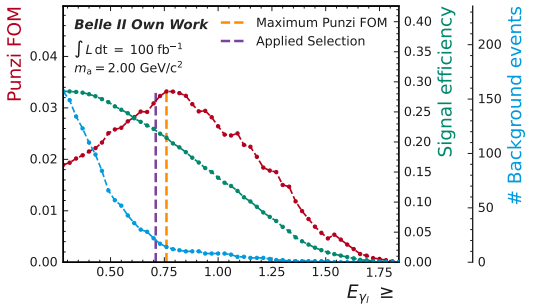

(c) Lower bound on E_{γ_l}.

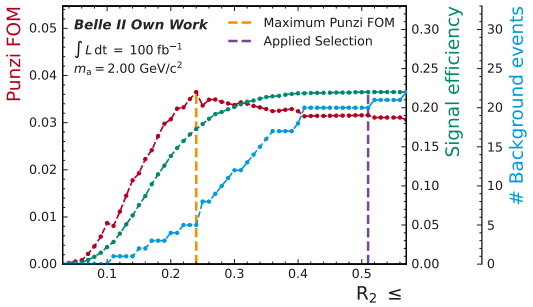

(d) Upper bound on R_2.

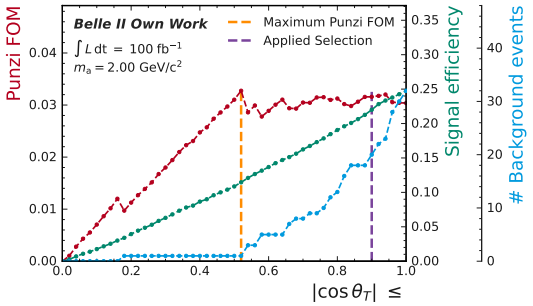

(e) Upper bound on $|\cos\theta_T|$.

Figure 4.14.: Punzi FOM (red dashed), signal efficiency (green dashed), and number of background events (blue dashed) as a function of the chosen selection for each scanned variable for an ALP with mass $m_\mathrm{a} = 2.0\,\mathrm{GeV/c^2}$. The optimization is performed with simulated events. With exception of the scanned variables, all the other ones are fixed to their optimized values. The orange, vertical line indicates the maximum of the Punzi FOM, the purple one the selection that was actually performed. The optimization was stopped early because the number of background events would have dropped too far otherwise.

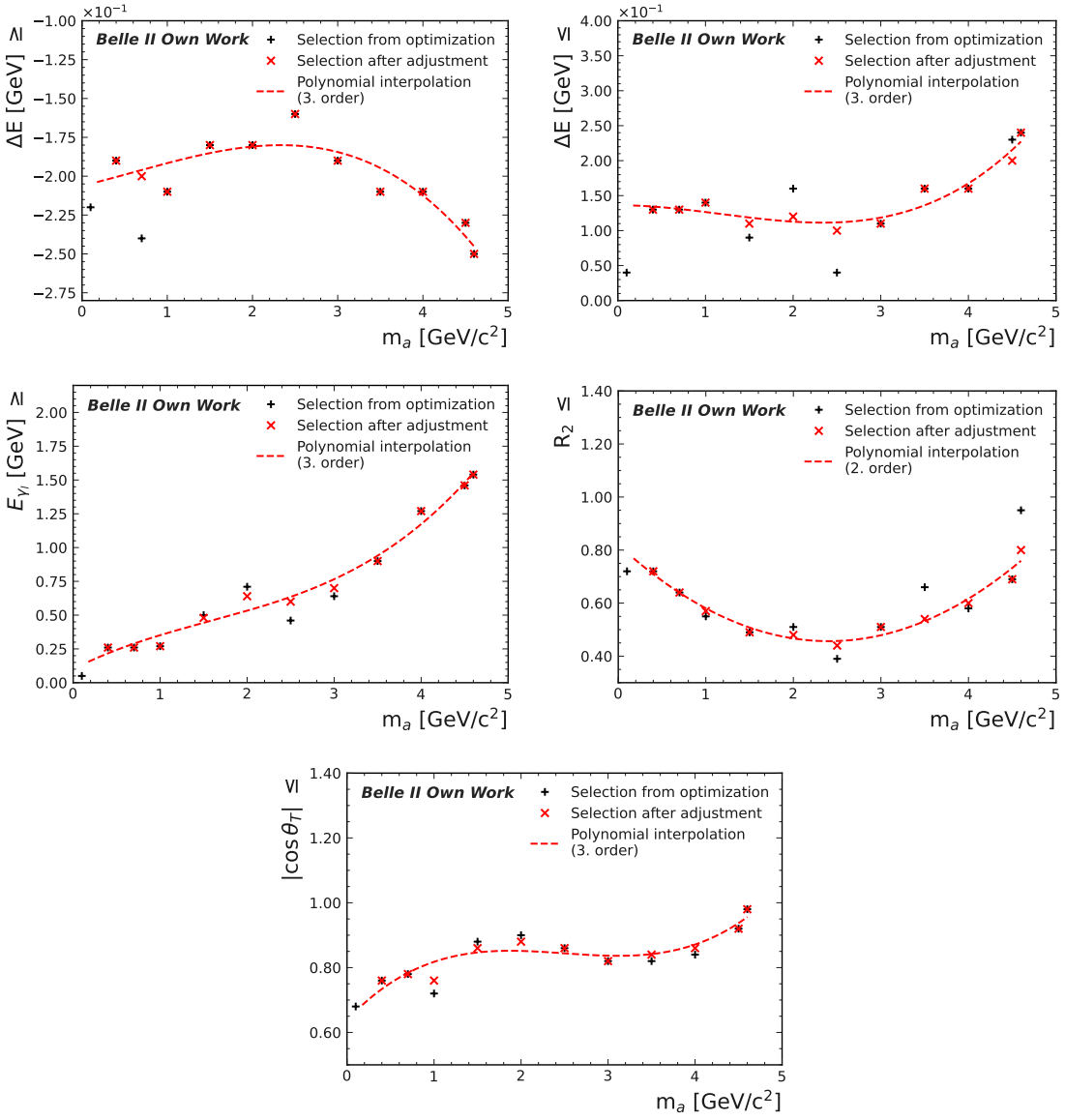

Figure 4.15.: The selections found by the Punzi optimization as a function of m_{a}. Some of the outlying selections were readjusted manually to ensure that they do not greatly affect the interpolation. Chebyshev polynomials are used for the interpolation, excluding the selections at $m_{\mathrm{a}} = 0.1\,\mathrm{GeV/c^2}$.

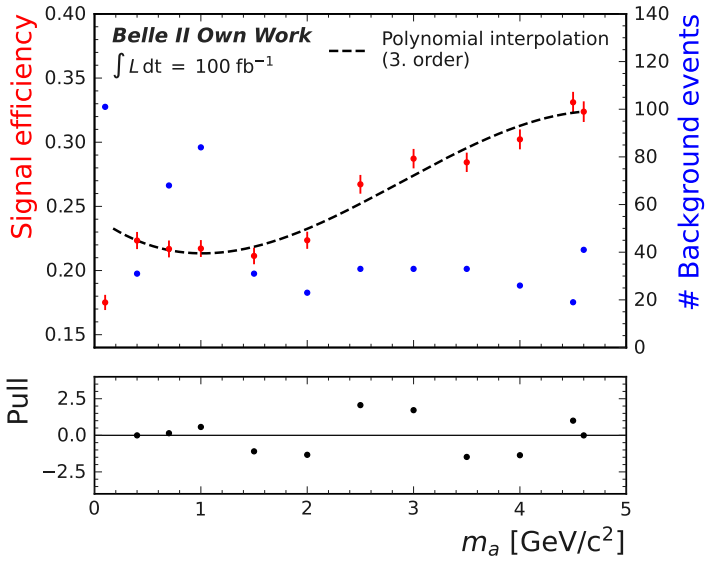

Figure 4.16.: Signal efficiency (red dots) and number of background events (blue dots) after applying all selections as a function of m_{a}. The events used are simulated. A polynomial interpolation (black dashed) is performed for the signal efficiency, excluding the signal efficiency at $m_{\mathrm{a}} = 0.1\,\mathrm{GeV/c^2}$. A pull plot belonging to the signal efficiency is shown below.

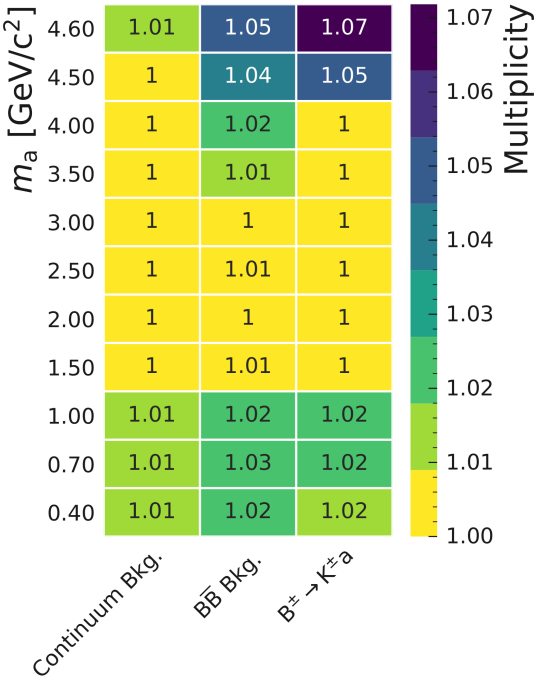

Figure 4.17.: Heatmap of the average number of candidates per event (multiplicity) for simulated signal and background events, plotted over m_{a}.

5. Signal Extraction

The goal of the search for the $B^{\pm} \to K^{\pm}a(\to \gamma\gamma)$ decay is to find and extract a signal or, in its absence, set an upper limit for it. To model the $M_{\gamma\gamma}$ distribution of the signal and extract the signal yield from it, it is fitted using the maximum likelihood method. The general concept of this method is presented in section 5.1. To analyze ALPs with different masses m_a, the expected signal pdfs in the $M_{\gamma\gamma}$ distribution must be determined for each m_a. This is described in section 5.2. The associated background modeling for each ALP mass hypothesis is discussed in section 5.3. Section 5.4 provides a discussion of potential systematic uncertainties and how they are quantified. An effect that gains importance in the case of a statistically significant observation is the so-called look-elsewhere effect. A description of this effect and how it is accounted for is given in section 5.5. The modeling of the combined signal + background pdf is tested to background-only pseudodata by calculating the significances for different ALP mass hypotheses in section 5.6. Finally, in section 5.7, upper limits for the background-only MC sample are computed to determine the simulation-based sensitivity of this analysis.

5.1. Maximum Likelihood Method

In particle physics experiments, the measurements are used to describe various particle properties like mass or momentum. Such properties are called observables. While the momentum of a particle takes different values, the mass of a particle is a fixed value. Due to the detector resolution, the mass distribution is spread around the true value.

The measured values of an observable x are randomly distributed and follow a probability density function (pdf) $f(x;\vec{\theta})$. It is assumed that the form of $f(x;\vec{\theta})$ is known. Here $\vec{\theta}$ is a set of unknown parameters that are estimated from a finite data sample by using the maximum likelihood method. For this purpose, the likelihood function

$$\mathcal{L}(\vec{\theta}) = \prod_{i=1}^{N} f(x_i;\vec{\theta}) \tag{5.1}$$

is defined, where $x_1, \ldots, x_N$ correspond to the measurements of the observable x. To estimate the unknown parameters $\vec{\theta} = \theta_1, \ldots, \theta_M$, the likelihood function is maximized by solving

$$\frac{\partial \mathcal{L}}{\partial \theta_i} = 0, \quad i = 1, \ldots, M \tag{5.2}$$

under the assumption that $\mathcal{L}$ is differentiable [34].

In reality, it is more common practice to minimize a function than to maximize it. In addition, it is computationally easier to calculate sums than products. Applying a minus sign and the logarithm to equation (5.1) results in the negative log-likelihood function

$$-\log \mathcal{L}(\vec{\theta}) = -\log\left(\prod_{i=1}^{N} f(x_i;\vec{\theta})\right) = -\sum_{i=1}^{N} \log f(x_i;\vec{\theta}), \tag{5.3}$$

which is minimized.

In this analysis, it is generally assumed that the number of observed events is a random value that is Poisson distributed with a mean value ν. It is estimated by multiplying the likelihood function in equation (5.1) with the Poisson distribution. This results in the extended likelihood function

$$\mathcal{L}(\nu,\vec{\theta}) = \frac{e^{-\nu}}{N!}\prod_{i=1}^{N} \nu f(x_i;\vec{\theta}). \tag{5.4}$$

An extended negative log-likelihood function can be derived from it as well. If ν does not depend on $\vec{\theta}$, the estimator $\hat{\nu}$ is equal to N. For further information about maximum likelihood fit and parameter estimation, the interested reader is referred to [34].

Throughout this analysis, this method is used to fit pdfs over given data samples and is provided by the ZFIT package [29]. It also provides the two methods HESSE and MINOS, which are used to calculate the uncertainties of the fit. MINOS provides asymmetric and more accurate errors and is generally used in this analysis to specify errors. HESSE is used for the interpolation (method of least squares) of fit parameters because it requires symmetric errors. More information about these methods can be found in [35].

5.2. Signal Fit

After applying the event selection from section 4.4, it is necessary to verify this has no major impact on the shape of the signal distribution $M_{\gamma\gamma}$. Otherwise, it could no longer be modeled well with a double sided crystal ball function. To verify this, the $M_{\gamma\gamma}$ distributions before and after applying all selections are juxtaposed. A fit is performed for both distributions and the double sided crystal ball parameters are extracted. Since the parameters $\alpha_{l/r}$ are highly correlated to $n_{l/r}$, the fit is stabilized by setting $n_{l/r} = 5$. Based on observations of previous fit values, this seems to be a good value for all m_{a}. Plots juxtaposing the fit parameters are displayed in figure 5.1. For some m_{a}, the corresponding $M_{\gamma\gamma}$ distributions are displayed in appendix B.1 to show them in a direct comparison.

The fit parameters for μ and σ have changed very slightly due to the event selection. On the other hand, α_l and α_r have a small offset compared to before. By looking at the individual distributions one recognizes that they still correctly follow a double sided crystal ball function. Its shape changed only slightly and is therefore neglected. As already shown in section 4.4 for the signal efficiency, the fit parameters are now interpolated as well. This is also shown in figure 5.1. This describes the expected signal distributions for the whole

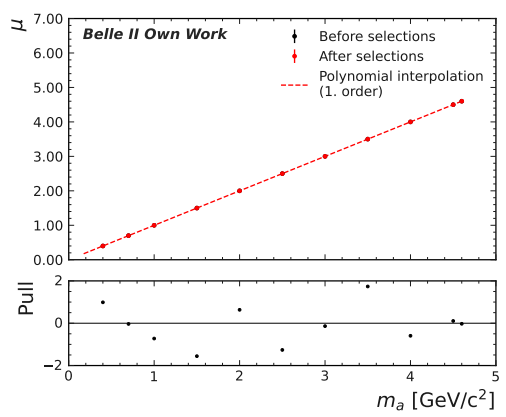

(a) Crystal ball parameter μ.

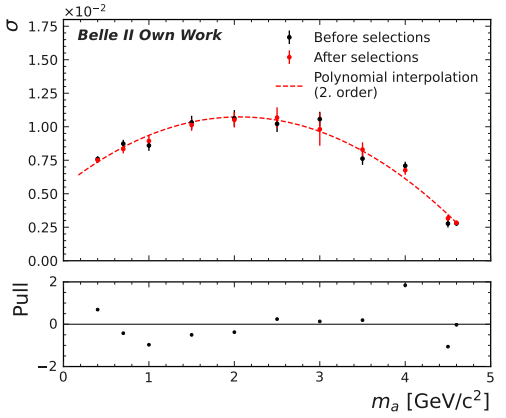

(b) Crystal ball parameter σ.

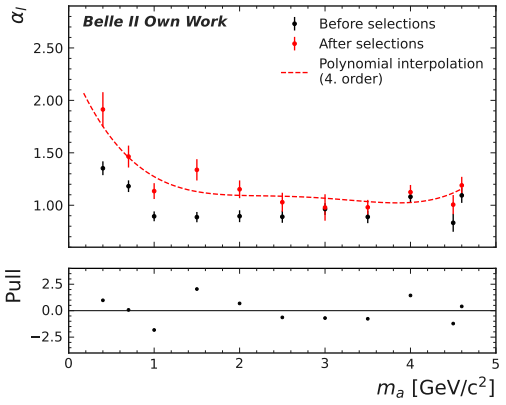

(c) Crystal ball parameter α_l.

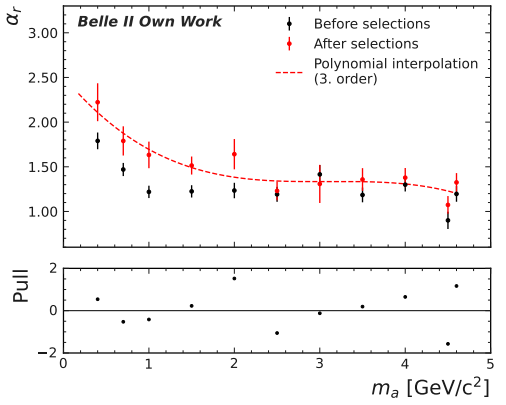

(d) Crystal ball parameter α_r.

Figure 5.1.: The signal fit parameters before (black) and after (red) applying the event selections from section 4.3. Chebyshev polynomials are used for interpolating the red signal fit parameters (red dashed). Pull plots belonging to the red fit parameters are shown below.

$M_{\gamma\gamma}$ spectrum. Chebyshev polynomials are used for interpolating the fit parameters. Pull plots are shown below to indicate the goodness of the interpolation. Note that from now on, when talking about the $M_{\gamma\gamma}$ distribution, the whole event selection is applied, if not stated otherwise.

To scan the $M_{\gamma\gamma}$ spectrum, the scan step size has to be chosen very small. Otherwise, any signal that may be present would be missed. A scan step size of $\sigma/2$ is chosen, taken from the interpolated signal fit parameters. The signal pdfs spaced by $\sigma/2$ are shown in figure 5.2. Only the range $m_\mathrm{a} \in [1.9, 2.1]\,\mathrm{GeV/c^2}$ is displayed, because σ is the largest in this region. The other regions are checked in this regard as well. It is recognizable that this scan step size is small enough to examine the entire $M_{\gamma\gamma}$ spectrum for $\mathrm{B}^\pm \to \mathrm{K}^\pm\mathrm{a}$ events.

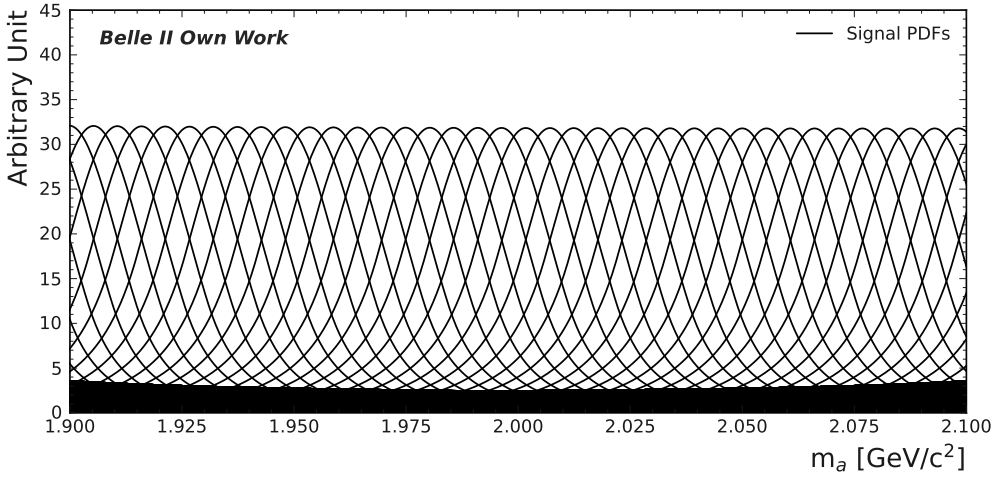

Figure 5.2.: Signal pdfs plotted in the scan step size of $\sigma/2$ from the interpolated double-sided crystal ball fits in figure 5.1. The range $m_{\mathrm{a}} \in [1.9, 2.1]\,\mathrm{GeV/c^2}$ is shown.

5.3. Background Fit

To extract the signal, not only the signal must be modeled well, but also the underlying background. In a few regions of the $M_{\gamma\gamma}$ distribution, the background is dominated by other processes, making the search for a new particle in those areas an extremely difficult task. The regions that are therefore excluded from this analysis are discussed in section 5.3.1. The selection of the background pdf and fit range in which the background is described are determined in section 5.3.2.

It should be noted at this point that a larger background MC sample corresponding to an integrated luminosity of $\int L\,\mathrm{dt} = 500\,\mathrm{fb}^{-1}$ is used now. After the event selection, there are too few events left of the $100\,\mathrm{fb}^{-1}$ sample considered so far. This would make it difficult to draw statistically significant conclusions in the next sections. The amount of background events of the new background MC sample corresponds to the amount of data that Belle II is expected to have recorded by summer 2022 [36].

5.3.1. Excluded Regions

As mentioned in section 2.4, peaking backgrounds arise from π^0, η, and η' decays at $M_{\gamma\gamma} \in \{0.135, 0.548, 0.958\}\,\mathrm{GeV/c^2}$. A signal peak at one of these masses would be very difficult to distinguish from the underlying background peak. Therefore, the corresponding regions are excluded from this analysis. The BaBar collaboration excluded the mass regions 0.10 - 0.175, 0.45 - 0.63, and 0.91 - 1.01 $\mathrm{GeV/c^2}$ for this purpose in its search [6]. It is checked whether these exclusion ranges are also useful in this study. Note that another resonance is also expected due to η_{c} decays. However, since no corresponding peak is observed in the $M_{\gamma\gamma}$ distribution, it is neglected in this analysis.

The selections for ALP masses (see section 4.4) at the π^0, η, and η' peaks are applied on the background MC sample. The distributions of the resonances follow a double-sided crystal

ball function. They are used here as a fake signal. The remaining distribution is modeled with a polynomial. By combining both pdfs, the $M_{\gamma\gamma}$ distribution is fitted. The result is displayed in figure 5.3. The regions in which the fitted peaks are located are excluded.

Distinct peaks are recognizable. The peak for η' consists of only a small number of events compared to the others. The exclusion ranges in this analysis are set to 0.09 - 0.175 $\mathrm{GeV/c^2}$, 0.48 - 0.61 $\mathrm{GeV/c^2}$, and 0.915 - 0.995 $\mathrm{GeV/c^2}$. Thus, the interval for π^0 is chosen slightly wider, for η and η' narrower, than specified by the BaBar collaboration. Due to differences between data and MC, the exclusion ranges may need to be readjusted. This could be done, for example, by analyzing a partially unblinded dataset.

5.3.2. Fit Range and Background PDF

To model the background distribution around a given ALP mass, a fit range has to be defined first. Due to the asymmetric shape of the signal distribution, the fit range should be selected in a way to take this into account. For this purpose, a fit is performed for the $M_{\gamma\gamma}$ distribution, and the 2 % to 98% inter-percentile range is computed. The distances between the μ parameter from the signal pdf to the borders of the inter-percentile range are calculated to define an asymmetric

$$\text{fit range} = \mu_{\mathrm{CB}}{}^{+x\cdot\mathrm{IPR}(0.98)}_{-x\cdot\mathrm{IPR}(0.02)}. \tag{5.5}$$

By multiplying a factor x, it is scaled to the desired fit range. The selection of this factor is not trivial and depends on the specification of the background pdf.

As pdf for fitting the background distribution, Chebyshev polynomials are chosen. The challenge now is to determine the polynomial order at each ALP mass hypothesis. This is not quite trivial, since the polynomial order also depends on the used fit range, which is not defined yet. However, by imposing some constraints, the problem is limited. One of them is that the polynomials should not exceed the 4th order. Otherwise, when applied to data, there is a risk of picking up an existing signal. The other constraint is the size of the fit range, which should be several multiples wider than the signal peak. This ensures that the shape of the pdf is not greatly affected by some local statistical fluctuations.

To determine the polynomial order, as well as the fit range size, a 5th order Chebyshev polynomial is performed with different fit ranges for all scan points in m_a. The fit range is adjusted until the 5th or even the 4th coefficient of the polynomial is around zero. This sets the size of the fit range. The other coefficients are used to define the order for each m_a. To visualize this, the individual coefficients are plotted as a function of m_a. With a fit range of 11 times the 2 % to 98% inter-percentile range of the signal distribution, the result shown in figure 5.4 is obtained. Only every 4th scan point is shown in the plot to avoid overloading the figure. Fluctuations are still evident at 4th and 5th order, especially for small ALP masses below 0.915 $\mathrm{GeV/c^2}$. Choosing an even smaller fit range does not make these fluctuations disappear either and should not be used because of the reasons mentioned before. For higher m_a, the fluctuations are less significant, but still present. For this reason, 3rd order polynomials are used for these m_a, although the 3rd coefficients are close to zero.

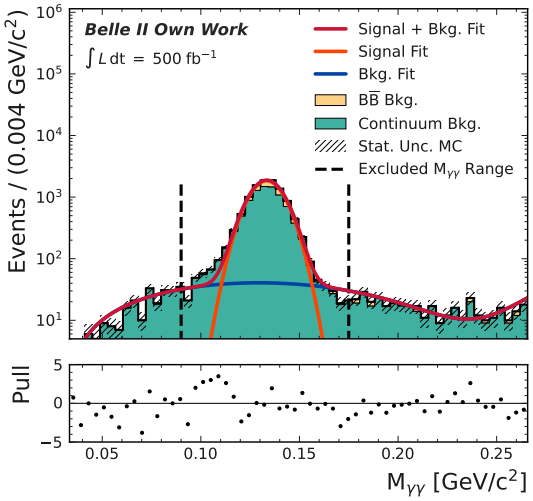

(a) π^0 peak.

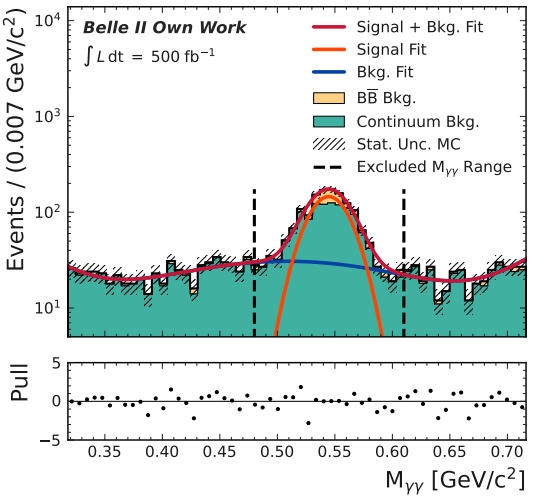

(b) η peak.

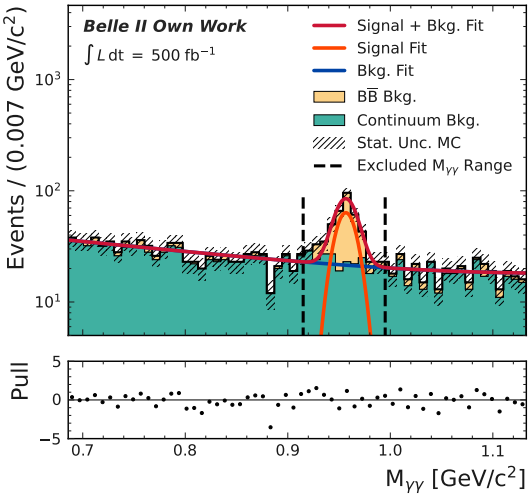

(c) η' peak.

Figure 5.3.: Peaking background distributions in $M_{\gamma\gamma}$ spectrum (simulation), originating from π^0, η, and η' mesons. A double-sided crystal ball pdf (orange, solid) and a polynomial pdf (blue, solid) are combined (red, solid) to fit the distributions. Pull plots belonging to the combined pdf are displayed below. The ranges 0.09 - 0.175 GeV/c^2, 0.48 - 0.61 GeV/c^2, and 0.915 - 0.995 GeV/c^2 (black, dashed) are excluded in this analysis.

A more detailed analysis of whether a 5th order polynomial should be used to model the background for $m_a < 0.915\,\mathrm{GeV/c^2}$ is presented. It is assumed that there are just statistical fluctuations in the $M_{\gamma\gamma}$ distribution, which lead to overfitting. To give the interested reader an impression of this, some $M_{\gamma\gamma}$ distribution with large/small values for c_5 are displayed in appendix B.2. Especially for light ALPs, the actual fit range is smaller due to the excluded regions in between. This makes them more susceptible to statistical fluctuations. To confirm

the assumption of overfitting, the goodness of fit is evaluated by performing a $\mathcal{X}^2$-Test. To compare different fit models, the reduced $\mathcal{X}^2$ for N bins is defined as

$$\mathcal{X}^2_{\text{red}} = \frac{\mathcal{X}^2}{\nu} = \frac{1}{\nu}\sum_{i=1}^{N}\left(\frac{y_i - f(x_i;\vec{\theta})}{\sigma_i}\right)^2 . \tag{5.6}$$

Here y_i corresponds to the value in bin i and $f(x_i;\vec{\theta})$ to the value of the background pdf at the position of bin i. A Poisson uncertainty $\sigma_i = \sqrt{y_i}$ is assumed on the value in bin i. ν describes the number of degrees of freedom and is the difference between the number of bins N and the order of the polynomial. Since the success of this method depends on the selected bin width, $\mathcal{X}^2_{\text{red}}$ is calculated several times for different bin widths. Bins with no entries are ignored. $\mathcal{X}^2_{\text{red}}$ is calculated for different polynomial orders in the 0.175 - 0.48 and 0.60 - 0.915 GeV/c^2 regions and compared. The result is that $\mathcal{X}^2_{\text{red}}$ is on average closer to 1 for a 4th order polynomial than for a 5th order polynomial and thus represents the better fit model. Therefore, the background distributions in these regions are fitted with a 4th order polynomial. More information about the model assessment and comparison with $\mathcal{X}^2_{\text{red}}$ can be found in [37].

5.4. Systematic Uncertainties

Even if much work is put into the generation of physics events, the detector simulation, and its response to all the different physics processes, in the end, there will still be differences between MC samples and real data from the detector. Such differences are systematic uncertainties that arise from many different sources during the whole analysis chain. Although systematic uncertainties are not considered in this analysis, they are mentioned in this section to show possible error sources. A summary of all possible uncertainties that could have an effect on this analysis is presented, along with ways to quantify them.

One uncertainty arises from the signal efficiency determination. In MC, the signal efficiency after the event selection and reconstruction is determined very precisely within its statistical uncertainties. In data, however, it is not clear whether the same amount of signal events would be triggered, reconstructed correctly, and survive the event selection. One way to estimate this uncertainty is by assuming a binomial uncertainty determined from MC simulations [38].

Another uncertainty comes from different signal shapes in MC and data. To account for this incorrect modeling, the signal pdf is convolved with a Gaussian pdf for some variation in the signal width. Logically this also affects the shape of the background distribution. Here, the fit for the background distribution is simply repeated with different models, such as higher-order polynomial fits. Because of the mis-modeling, the size of the fit range is also subject to systematic uncertainty. Its size is simply increased by a few percent and the fit is repeated. The difference between the two fits is taken as a systematic uncertainty. The luminosity, PID, track reconstruction efficiency, and photon reconstruction efficiency also have systematic uncertainties, that affect this measurement. They will be provided by the Belle II Collaboration at the end of the data taking period.

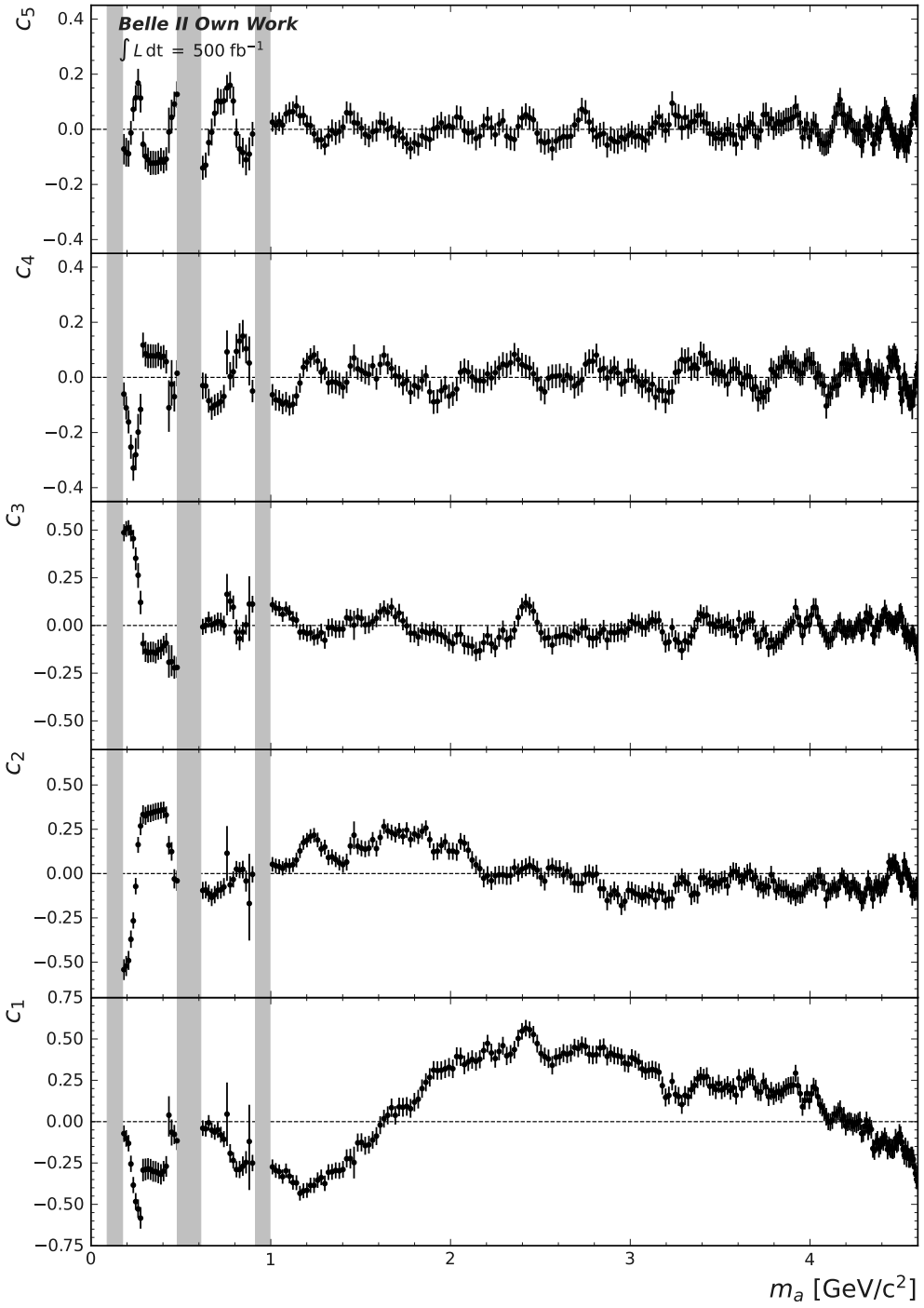

Figure 5.4.: Coefficients of a 5th order Chebyshev polynomial fit as a function of m_{a}. The fit range is defined as 11 times the 2 % to 98% inter-percentile range of the signal distribution (see equation (5.5)). The gray vertical bands indicate the exclusion ranges of this analysis.

Similar to the study of the BaBar Collaboration, the likelihood function is convolved with a Gaussian with a width equal to the systematic uncertainty to account for it in the limit calculation [6]. In contrast to particles such as neutrinos, photons and kaons leave distinct signatures in the detector. Therefore, it is reasonable to assume that they are simulated properly. In that case, almost none of the listed systematic uncertainties would dominate the search for the $B^{\pm} \to K^{\pm}a(\to \gamma\gamma)$ decay. However, the systematic uncertainties on the signal and background pdfs are not easy to estimate and could indeed have a crucial effect.

5.5. Look-Elsewhere Effect

When searching for a signal in a large parameter space, the probability of making a statistically significant observation by chance is high even if there are no signal events involved. Such discrepancies come from background fluctuations and their occurrences increase with the size of the parameter space being investigated. This is called the look-elsewhere effect. This effect must be taken into account if such an excess is observed in data. Two methods of dealing with this are outlined in this section. The explanations are based on [39, 40]

The most obvious idea to address this problem is to produce more background-only MC. This is used to look for more fluctuations that imitate a signal. This would be a simple and also correct method to analyze this effect. However, it would have to be repeated $\mathcal{O}(10^7)$ times to observe significances above 5σ and would thus be computationally expensive. Therefore, it is worth considering another method for this.

The probability p_{local} of observing a fake signal with a specified significance at a given mass point is calculated. As an example, a significance of $Z = 5\sigma$ is used. This is compared to the probability p_{global} of observing a fake signal of equal significance anywhere in the mass spectrum. While the first one is quite easy to determine, the second one is much more difficult to obtain. Fortunately, there is a relation that can be used for approximation. It is defined as

$$p_{\text{global}} \approx p_{\text{local}} + \langle N(c) \rangle, \tag{5.7}$$

where $\langle N(Z) \rangle$ denotes the average number of "upcrossings" that exceed the 5σ significance. Note that MC samples for neighboring scan points are very similar, making the observed significances not independent of each other. If there is a great significance at scan point i, the chance for a great significance at $i + 1$ is high as well. For example, if four neighboring scan points are above c, they are counted as one upcrossing instead of four.

Now c is chosen quite high in this example. Similar to the first method, a large number of toy MC would be required to determine $\langle N(Z) \rangle$. Toy MC are random samples generated based on a predefined pdf. Choosing a smaller threshold $Z_0 = 0.5\sigma$ and counting the number of upcrossings there, $\langle N(Z) \rangle$ is approximated by

$$\langle N(Z) \rangle \approx \langle N(Z_0) \rangle e^{-(Z - Z_0)/2}. \tag{5.8}$$

This reduces the number of required toy MC for calculating p_{global} to a minimum. Thus, before falsely claiming a discovery, the local significance must be converted to a global one, to take the look-elsewhere effect into account.

5.6. Significance Scan

The explanations in this section are based on [1] and [5, chapter 40].

In particle physics searches, it is tested whether a measurement is consistent with a predefined hypothesis. Such a hypothesis could be that the observed data are produced only by Standard Model processes. This is also called null hypothesis H_0 or background-only hypothesis. To describe new physics one or more alternative hypotheses H_1 are defined, which describe the observation

$$N_{\text{obs}} = \mu N_{\text{sig}} + N_{\text{bkg}} \tag{5.9}$$

as a combination of signal and background events. Here μ denotes the signal strength parameter. It is zero when considering H_0 and one in case of H_1. To claim a discovery, the null hypothesis must be rejected based on the observed data. The significance indicates the extent to which the measurement deviates from the tested hypothesis.

A pdf is constructed for each of the hypotheses and fitted over the measured distribution. The signal pdf and its corresponding parameters were introduced in section 5.2. The parameters at each m_{a} are fixed to their interpolated values. The only free parameter is the signal yield. This is different for the background pdf. Here only the polynomial order is fixed. Its coefficients and yield are free parameters. By adding the signal and background pdf, a combined pdf is obtained, which is fitted over the previously defined $M_{\gamma\gamma}$ fit range.

The probability of obtaining N_{obs} or more events under the assumption of H_0 is described by the so-called p-value. The smaller this value is, the less a correct description of N_{obs} is given by H_0. The significance Z is calculated via

$$Z = \Phi^{-1}(1 - \text{p-value}), \tag{5.10}$$

where Φ^{-1} is the inverse cumulative distribution function of a standard Gaussian distribution. The significance is computed at all scan points in m_{a}. Here, μ is not restricted to be ≥ 0 in order to obtain negative significances as well. If there are strong fluctuations in one direction, it indicates a problem with the fit. The significance as a function of m_{a} is shown in figure 5.5. The fitted signal yield N_{sig} is also displayed to show how many events produce a corresponding significance.

Overall, the number of upward and downward fluctuations is very similar. However, from $4.0\,\text{GeV/c}^2$ a trend of increasing downward fluctuations is seen. For $m_{\text{a}} = 0.671\,\text{GeV/c}^2$ and $m_{\text{a}} = 4.539\,\text{GeV/c}^2$ there are accesses down to -3σ visible. One upward fluctuation for $m_{\text{a}} = 2.259\,\text{GeV/c}^2$ is observed, which barely reaches a significance of 3σ. Plots showing the $M_{\gamma\gamma}$ distributions belonging to the two highest and two lowest significances are displayed in figure 5.6.

A total of 1078 fits are performed for the entire $M_{\gamma\gamma}$ spectrum. As in section 5.5, it is not surprising to make such an observation with so many measurements. To check if these are just statistical fluctuations or occur systematically, additional MC samples could be used. If fluctuations still occur at the same locations, further investigations would have to be conducted. However, there is some evidence that these are just statistical fluctuations (see appendix C). Therefore, they are neglected at this point and the analysis is continued.

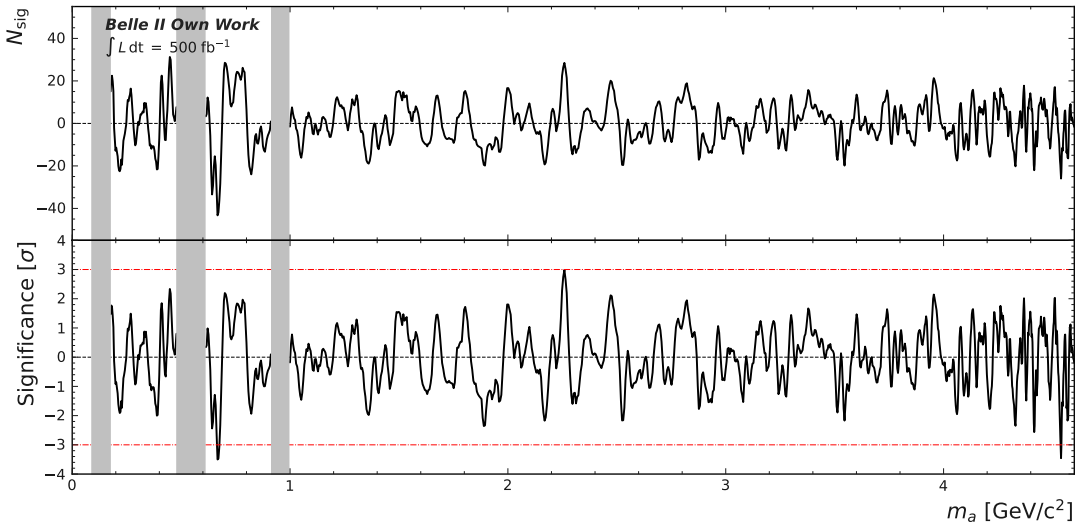

Figure 5.5.: Observed signal yield N_{sig} and significance of simulated background-only pseudodata as function of m_{a}. The black dashed lines are aligned to $N_{\text{sig}} = 0$ and 0σ significance, to better visualize the fluctuations around these points. The red dash-dotted lines indicate a significance of $\pm 3\sigma$ for a better estimation of the magnitudes of the fluctuations. The gray vertical bands indicate the exclusion ranges of this analysis.

5.7. Simulation-based Sensitivity

A description of the probability of a discovery, should a signal be present in data, is given by the expected sensitivity. In case of the absence of $\mathrm{B}^{\pm} \to \mathrm{K}^{\pm}\mathrm{a}(\to \gamma\gamma)$ events, it indicates which values of the signal strength parameter μ may be excluded. The explanations in this section are based on [5, chapter 40].

The simulation-based sensitivity of this analysis is examined using the $\mathrm{CL_S}$ method. For this purpose, the two p-values p_0 and p_1 are determined under the assumption of the corresponding hypotheses H_0 and H_1. The modified confidence level

$$\mathrm{CL_S} = \frac{p_1}{1 - p_0} \tag{5.11}$$

is obtained from the ratio of the two p-values. Suppose that in a measurement the number of observed events N_{obs} is approximately equal to the expected background N_{bkg}. Thus, the evidence for an existing signal is very low. If $\mathrm{CL_S}$ is smaller than a predetermined value α, then N_{sig} is excluded at a $1 - \alpha$ confidence level (CL). This is then an upper limit on N_{sig}. To compare the result with that obtained from the BaBar study, a CL of 90 % is used [6].

However, since many other preparations have to be made first before looking at data, the $\mathrm{CL_S}$ method is still useful to determine the simulation-based sensitivity of this analysis. Similar to the previous section, a combined pdf is created from the signal and background pdfs. The combined pdf is used to perform a fit over the background-only $M_{\gamma\gamma}$ distribution. They are performed throughout the $M_{\gamma\gamma}$ distribution in steps of half the σ parameter of

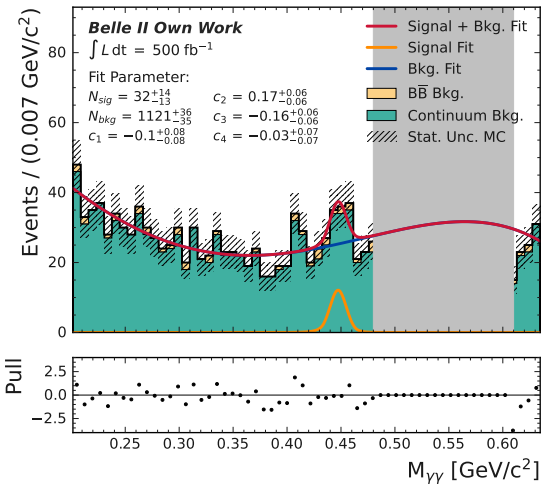

(a) $m_{\mathrm{a}} = 0.448\,\mathrm{GeV/c^2}$.

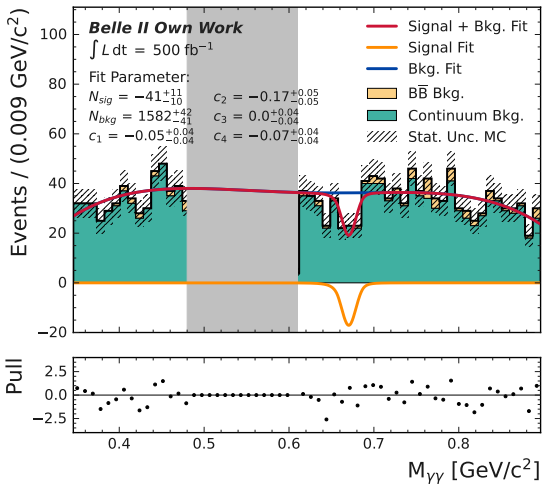

(b) $m_{\mathrm{a}} = 0.671\,\mathrm{GeV/c^2}$.

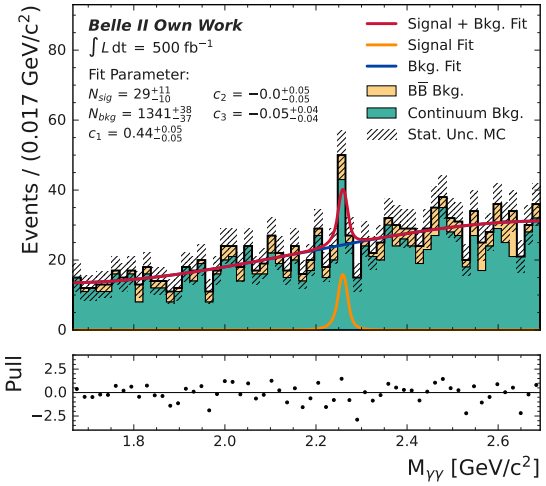

(c) $m_{\mathrm{a}} = 2.259\,\mathrm{GeV/c^2}$.

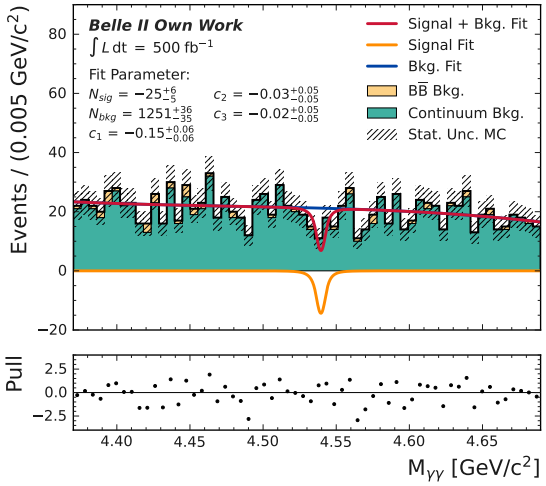

(d) $m_{\mathrm{a}} = 4.539\,\mathrm{GeV/c^2}$.

Figure 5.6.: $M_{\gamma\gamma}$ distributions from the background-only MC sample, associated to the two largest and two smallest significances in figure 5.5. The displayed $M_{\gamma\gamma}$ range in each histogram corresponds to the fit range. A combined signal and background fit (orange) is performed for $M_{\gamma\gamma}$. The signal (red) and background (blue) components of the fit are displayed. The parameters from the combined fit are shown on the left side of each histogram. A pull plot belonging to the combined fit is displayed underneath. A Poisson uncertainty is assumed for each bin and indicated by a black dashed box. The gray vertical bands indicate the exclusion range around the η mass.

the signal distribution. This time $N_{\text{sig}} \geq 0$ is required, since a peak in the distribution is expected in the presence of a signal. The statistical fluctuations in the background MC sample are perceived as a fake signal by the fit. The observed limits under the H_1 hypothesis and the expected limits under H_0 are computed. Detailed descriptions of the used method can be found in [41].

However, one is less interested in upper limits for N_{sig}, but rather in limits for the branching fraction

$$\mathcal{B}(\mathrm{B}^{\pm} \to \mathrm{K}^{\pm}\mathrm{a}(\to \gamma\gamma)) = \frac{N_{\text{sig}}}{2\epsilon_{\text{sig}} \cdot N_{\mathrm{B}^{+}\mathrm{B}^{-}}}. \tag{5.12}$$

Here, ϵ_{sig} describes the signal efficiency belonging to the corresponding m_{a} and

$$N_{\mathrm{B}^{+}\mathrm{B}^{-}} = \sigma(\mathrm{e}^{+}\mathrm{e}^{-} \to \mathrm{B}^{+}\mathrm{B}^{-}) \cdot L_{\text{int}} = 2.7 \cdot 10^{8} \tag{5.13}$$

is the amount of produced $\mathrm{B}^{+}\mathrm{B}^{-}$ events at an integrated luminosity of $500\,\mathrm{fb}^{-1}$ [5, 25]. By substituting the limits for N_{sig}, the limits for the branching fraction are obtained. The result is displayed in figure 5.7. There are two plots shown. The lower one is just a zoomed-in version of the upper one so that the structures in the area of small ALP masses can be seen better. It is noticeable that the limit jumps back and forth near the exclusion ranges. This is caused by the fit range starting to include more and more events on the other side of the exclusion range. In some cases, this leads to a great change of the background pdfs of two neighboring scan points. Due to the lower signal efficiency near an exclusion range, the upper limit goes up there.

Due to the wide scan area and the very narrow signal peak, a large number of fluctuations are observed. But overall they behave within the bounds of what one would expect. With increasing ALP mass, the simulation-based sensitivity on the branching fraction $\mathcal{B}(\mathrm{B}^{\pm} \to \mathrm{K}^{\pm}\mathrm{a}(\to \gamma\gamma))$ increases continuously. With a value of $\sim 10^{-7}$ achieved in this analysis, it is comparable to the current limit from the BaBar collaboration (see section 2.4). But as mentioned in section 5.4, no systematic uncertainties have been taken into account, which would have an impact on the result.

The event selection in chapter 4 is optimized for a background MC sample of $100\,\mathrm{fb}^{-1}$. The optimization is stopped early as soon as the number of background events drops below a certain value. This is observed for half of the analyzed signal MC samples. An optimization with a background MC sample of $500\,\mathrm{fb}^{-1}$ would consequently lead to tighter selections and a better background separation. However, this has not been done to ensure that enough events are kept to fit the background distribution. Gaps in the distribution would also lead to problems in section 5.6, since strong downward fluctuations would be observed in the significance scan (as shown in appendix C). The best would be to use all the available background MC samples, weight them down to $500\,\mathrm{fb}^{-1}$ and repeat the previous analysis steps with them.

The BaBar collaboration used two boosted decision trees (BDTs) to perform their event selection to separate the different types of backgrounds. That, or using neural networks, would be further options for achieving even better expected sensitivities.

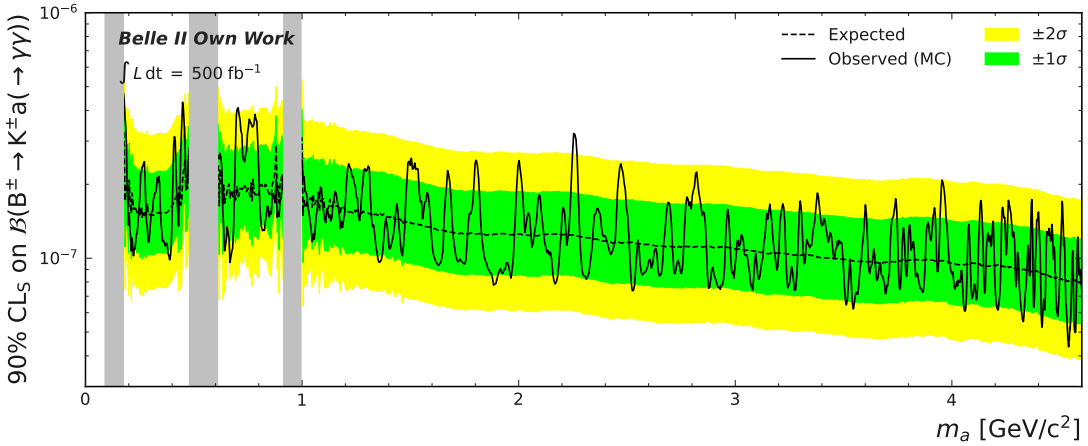

(a) 90% $\mathrm{CL_S}$ in range 0.0 - 4.60 $\mathrm{GeV/c^2}$

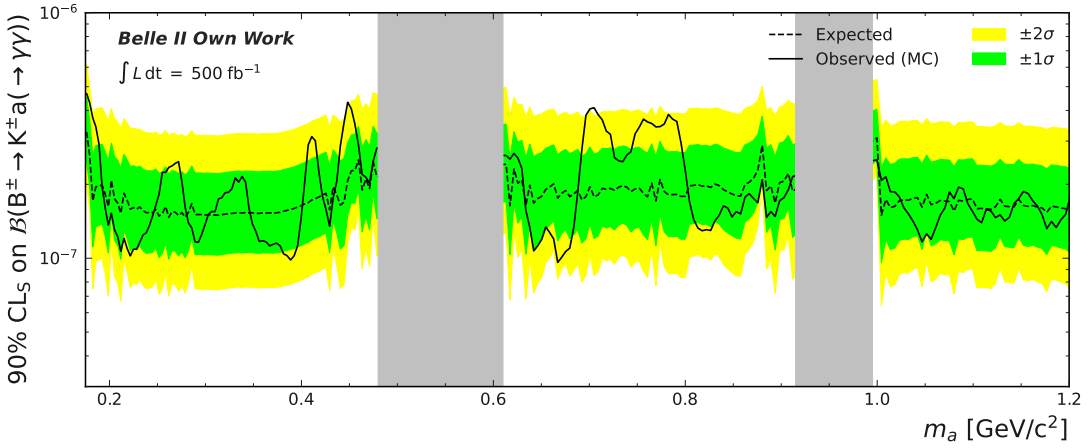

(b) 90% $\mathrm{CL_S}$ in range 0.175 - 1.20 $\mathrm{GeV/c^2}$

Figure 5.7.: Upper limits on the branching fraction $\mathcal{B}(\mathrm{B}^\pm \to \mathrm{K}^\pm\mathrm{a}(\to \gamma\gamma))$ at a CL of 90 % for simulated background-only pseudodata as a function of the scanned ALP mass m_a. The black solid line denotes the observed upper limit with the assumption of H_1 and the black dashed line the expected upper limit under H_0. The green and yellow bands correspond to ± 1 and ± 2 times the standard deviation σ of the expected limit. The gray vertical bands indicate the exclusion ranges of this analysis. The lower plot is a zoomed-in version of the upper one to better visualize the lower ALP mass region.

6. Conclusion and Outlook

In this thesis, the simulation-based sensitivity study of short-lived ALPs from the decay $B^{\pm} \to K^{\pm}a(\to \gamma\gamma)$ is presented. This decay allows us to study the coupling of ALPs with W bosons. Only short-lived ALPs are considered, which decay into two photons immediately after their production.

The simulation-based search is performed in the mass range $0.175 \leq m_a \leq 4.60\,\mathrm{GeV/c^2}$. The event selection is optimized for 12 signal MC samples with different m_a and for a background MC sample corresponding to $100\,\mathrm{fb}^{-1}$ of integrated luminosity. First, some loose preselections are applied in the event reconstruction. The selection is optimized for each signal MC sample around the expected signal peak in the $M_{\gamma\gamma}$ distribution. To obtain a more distinct signal peak and reduce the number of underlying background events, a mass constrained fit is applied to $M_{\gamma\gamma}$. Subsequently, a set of variables is determined that show excellent separation between signal and background events. The selections on these variables were optimized for the different signal MC samples using the Punzi figure of merit as a benchmark. For this purpose, an optimization algorithm is designed that takes the correlation of the different variable selections into account and does not impose a fixed selection order. To analyze ALPs in the whole $M_{\gamma\gamma}$ spectrum, the signal efficiency and the optimized selections are interpolated.

Subsequently, the signal extraction is discussed. As stated in section 5.3, a background MC sample corresponding to $500\,\mathrm{fb}^{-1}$ is used here. The signal fit parameters are interpolated after applying the optimized selections. Signal pdfs for the whole $M_{\gamma\gamma}$ spectrum are determined from the interpolation. For each ALP mass hypothesis, the fit range and background pdf for fitting the $M_{\gamma\gamma}$ distribution are determined. The ranges 0.09 - $0.175\,\mathrm{GeV/c^2}$, 0.48 - $0.61\,\mathrm{GeV/c^2}$, and 0.915 - $0.995\,\mathrm{GeV/c^2}$ are excluded due to peaking backgrounds caused by π^0, η, and η' decays. A signal + background fit is used to determine the significance of background-only pseudodata for each ALP mass hypothesis. To test the robustness of the fit, the number of observed signal events N_{sig} is allowed to be < 0. Finally, the simulation-based sensitivity is determined by computing upper limits on background-only pseudodata.

The next step to do for this study is to perform toy MC studies to verify the validity of the signal extraction method for different ALP masses. Subsequently, sideband studies will be performed in the region $M_{\mathrm{bc}} < 5.26\,\mathrm{GeV/c^2}$ and control channels such as $B^{\pm} \to K^{\pm}\eta$ will be investigated. From the results, correction factors will be determined and applied to the MC samples. Another possibility would be to include the results of these studies as

systematic uncertainties in the fit. As discussed in section 5.4, except for the systematic uncertainties on the signal and background pdfs, the search for the $B^{\pm} \to K^{\pm}a(\to \gamma\gamma)$ decay is not expected to be dominated by systematic uncertainties.

With an MC sample corresponding to $500\,\mathrm{fb}^{-1}$, a simulation-based sensitivity of $\sim 10^{-7}$ on the branching fraction $\mathcal{B}(B^{\pm} \to K^{\pm}a(\to \gamma\gamma))$ is achieved. This is comparable to the current limit from the BaBar collaboration (see section 2.4). However, there is still room for improvement. By using signal MC samples for more ALP masses, more accurate interpolations in section 4.4 and section 5.2 could be achieved. Furthermore, it could be investigated what sensitivities are achieved below $0.09\,\mathrm{GeV/c^2}$ or between 4.6 - $4.78\,\mathrm{GeV/c^2}$. The event selection in section 4.3 could be also improved by using boosted decision trees or neural networks. This would increase the simulation-based sensitivity even further. As a result, there is a good chance for the Belle II experiment to decrease the upper limits on $\mathcal{B}(B^{\pm} \to K^{\pm}a(\to \gamma\gamma))$ in further studies.

Acronyms

ALP axion-like particle

CB Crystal Ball

CDC Central Drift Chamber

CL confidence level

ECL Electromagnetic Calorimeter

FCNC flavor-changing neutral current

IP interaction point

MC Monte Carlo

pdf probability density function

Punzi FOM Punzi figure of merit

QCD quantum chromodynamics

ROE rest of event

SM Standard Model

A. Punzi Optimization - Control Plots

Some additional control plots for the Punzi optimization from section 4.3.3 are shown in figure A.1, figure A.2, and figure A.3.

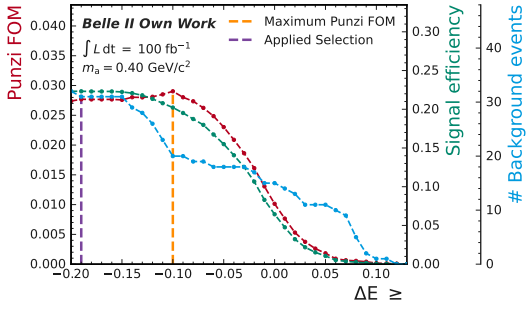

(a) Lower bound on ΔE.

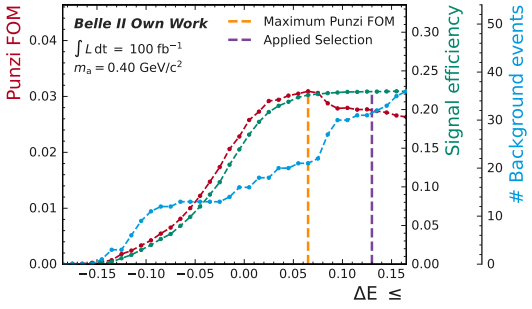

(b) Upper bound on ΔE.

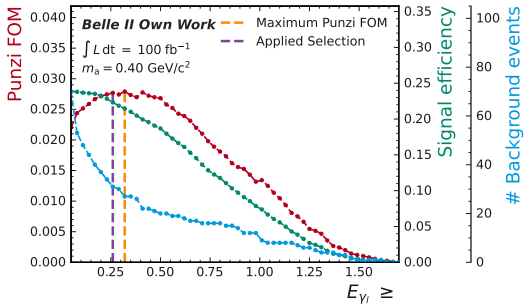

(c) Lower bound on E_{γ_l}.

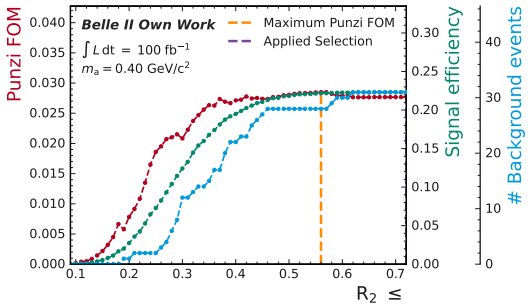

(d) Upper bound on R_2.

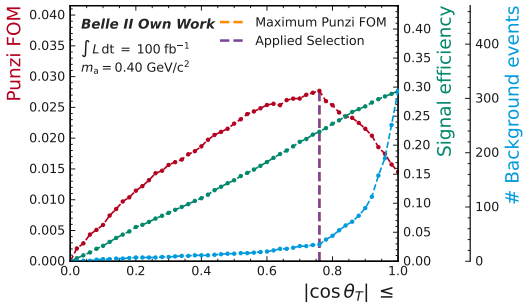

(e) Upper bound on $|\cos\theta_T|$.

Figure A.1.: Punzi FOM (red dashed), signal efficiency (green dashed), and number of background events (blue dashed) as a function of the chosen selection for each scanned variable for an ALP with mass $m_a = 0.4\,\mathrm{GeV/c^2}$. The optimization is performed with simulated events. With exception of the scanned variables, all the other ones are fixed to their optimized values. The orange, vertical line indicates the maximum of the Punzi FOM, the purple one the selection that was actually performed.

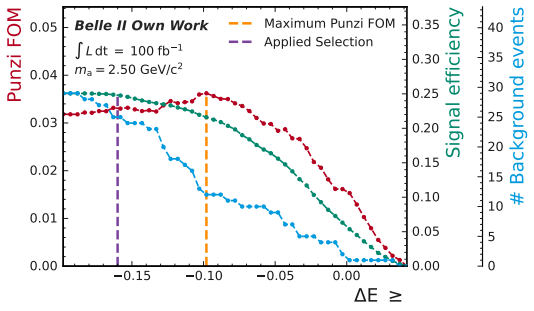

(a) Lower bound on ΔE.

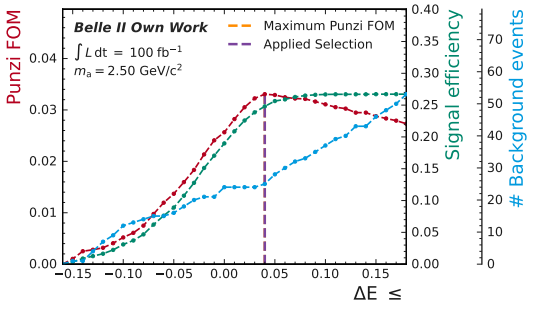

(b) Upper bound on ΔE.

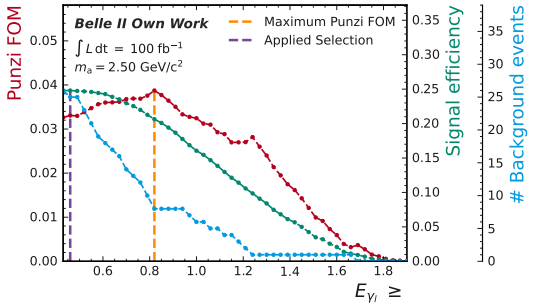

(c) Lower bound on E_{γ_l}.

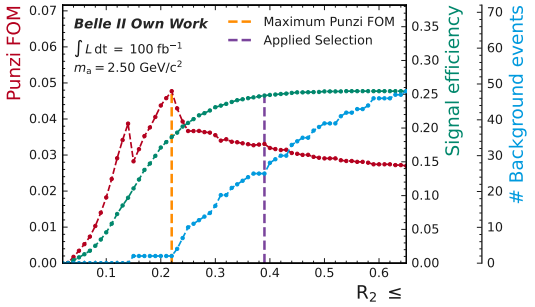

(d) Upper bound on R_2.

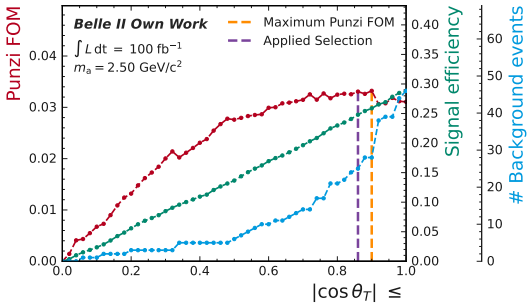

(e) Upper bound on $|\cos\theta_T|$.

Figure A.2.: Punzi FOM (red dashed), signal efficiency (green dashed), and number of background events (blue dashed) as a function of the chosen selection for each scanned variable for an ALP with mass $m_\mathrm{a} = 2.5\,\mathrm{GeV/c^2}$. The optimization is performed with simulated events. With exception of the scanned variables, all the other ones are fixed to their optimized values. The orange, vertical line indicates the maximum of the Punzi FOM, the purple one the selection that was actually performed.

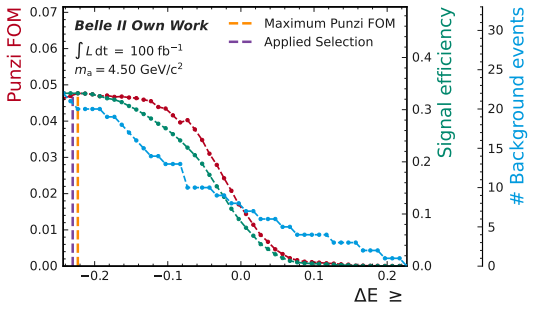

(a) Lower bound on ΔE.

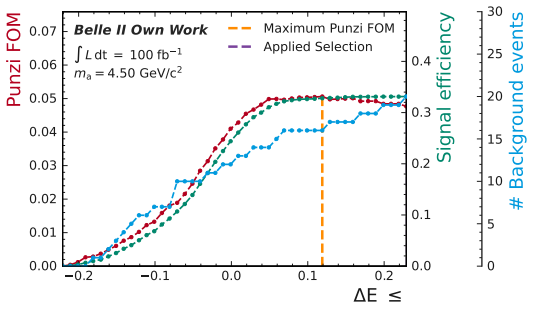

(b) Upper bound on ΔE.

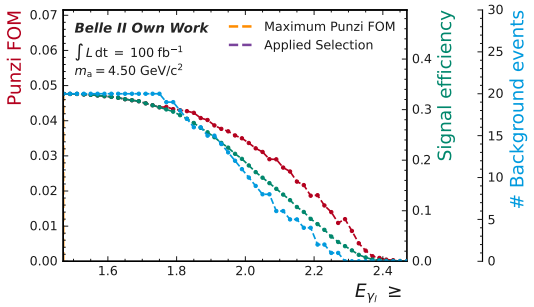

(c) Lower bound on E_{γ_l}.

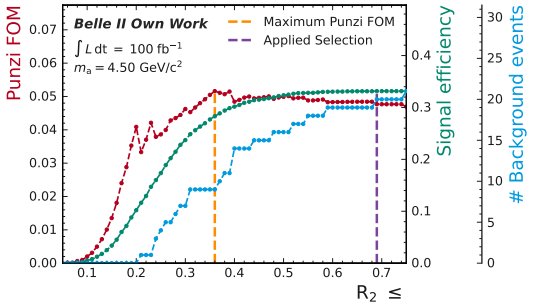

(d) Upper bound on R_2.

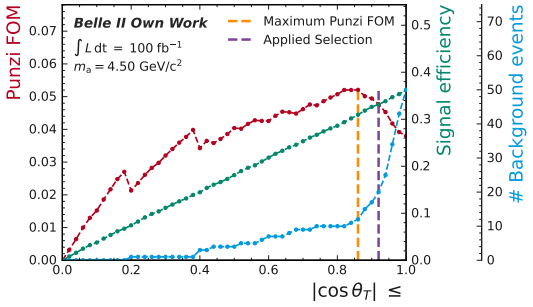

(e) Upper bound on $|\cos\theta_T|$.

Figure A.3.: Punzi FOM (red dashed), signal efficiency (green dashed), and number of background events (blue dashed) as a function of the chosen selection for each scanned variable for an ALP with mass $m_\mathrm{a} = 4.5\,\mathrm{GeV/c^2}$. The optimization is performed with simulated events. With exception of the scanned variables, all the other ones are fixed to their optimized values. The orange, vertical line indicates the maximum of the Punzi FOM, the purple one the selection that was actually performed.

B. Additional $M_{\gamma\gamma}$ Distributions

B.1. Distribution after Selection

Comparison of the $M_{\gamma\gamma}$ distributions of some signal MC samples after performing the event reconstruction from section 4.1 and after applying the full selection from section 4.4. They are displayed in figure B.1 for $0.4\,\mathrm{GeV/c^2}$, $2.0\,\mathrm{GeV/c^2}$, and $4.5\,\mathrm{GeV/c^2}$ ALPs.

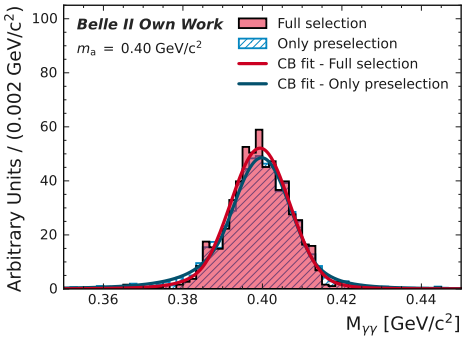

(a) $m_\mathrm{a} = 0.4\,\mathrm{GeV/c^2}$.
Displayed range: $[0.35, 0.45]\,\mathrm{GeV/c^2}$.

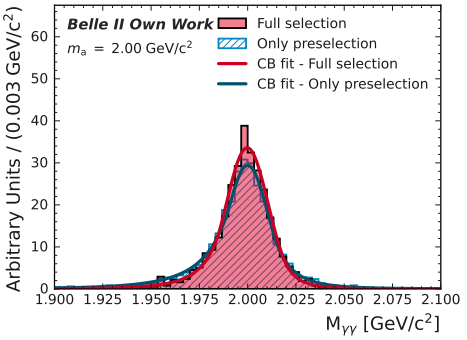

(b) $m_\mathrm{a} = 2.0\,\mathrm{GeV/c^2}$.
Displayed range: $[1.9, 2.1]\,\mathrm{GeV/c^2}$.

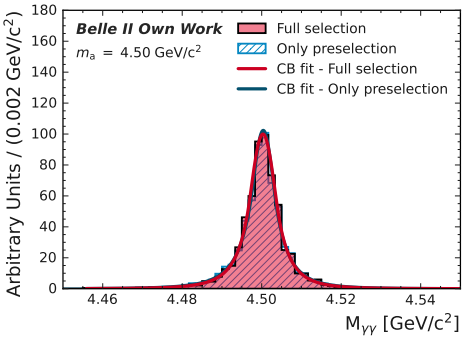

(c) $m_\mathrm{a} = 4.5\,\mathrm{GeV/c^2}$.
Displayed range: $[4.45, 4.55]\,\mathrm{GeV/c^2}$.

Figure B.1.: $M_{\gamma\gamma}$ distributions of simulated $\mathrm{B^\pm} \to \mathrm{K^\pm a}(\to \gamma\gamma)$ events after the event reconstruction (red) and after applying the full event selection (blue). Double-sided CB fits are performed for both distributions.

B.2. Background Fit Comparison

Some $M_{\gamma\gamma}$ distributions of the background-only MC sample are displayed in figure B.2. The distributions for the ALP mass hypotheses are shown, for which large/small values for the coefficient c_5 of a polynomial fit are observed (see section 5.3). For comparison, a 4th and 5th order polynomial are fitted to the distributions.

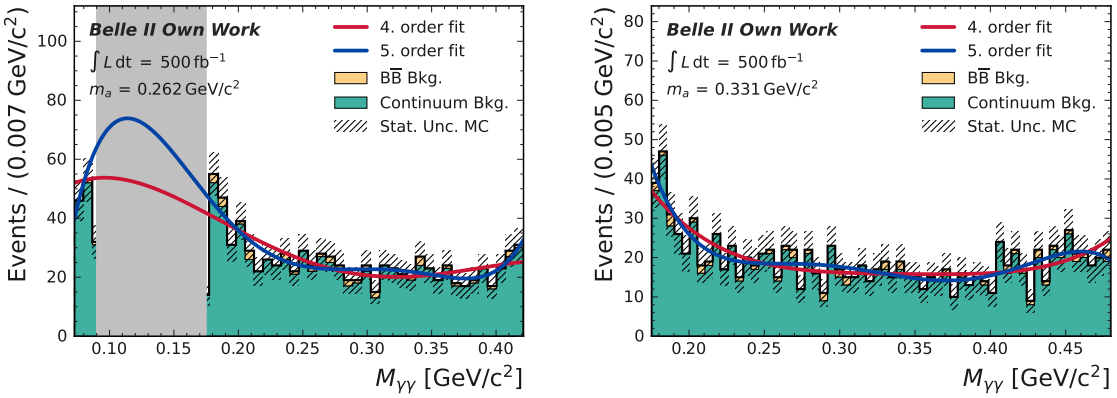

(a) $m_a = 0.262\,\text{GeV/c}^2$.

(b) $m_a = 0.331\,\text{GeV/c}^2$.

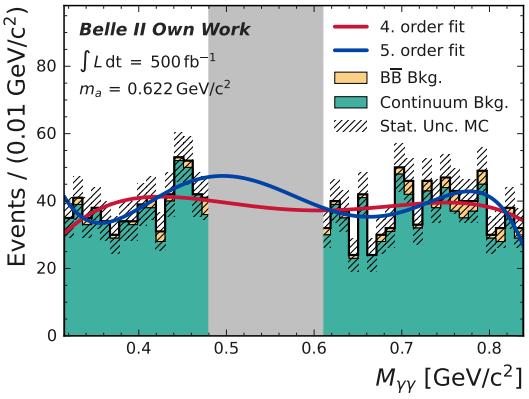

(c) $m_a = 0.622\,\text{GeV/c}^2$.

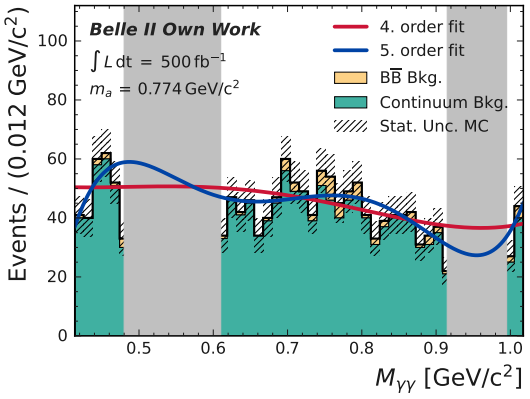

(d) $m_a = 0.774\,\text{GeV/c}^2$.

Figure B.2.: $M_{\gamma\gamma}$ distributions from the background-only MC sample, associated to the two largest and two smallest values for c_5 in Figure 5.4. The displayed $M_{\gamma\gamma}$ range in each histogram corresponds to the fit range. A 4th order (red) and 5th order polynomial fit are performed for $M_{\gamma\gamma}$. A Poisson uncertainty is assumed for each bin and indicated by a black dashed box. The gray vertical bands indicate the exclusion range around the π^0, η, and η' masses.

C. Significance scan for different background MC samples

The significance scan from section 5.6 is repeated for different independent background MC samples. The $500\,\mathrm{fb}^{-1}$ MC sample is divided into five sub-samples with $100\,\mathrm{fb}^{-1}$ each. The result of the scan is shown in figure C.1. Some strong downward fluctuations are observed. Some significances even drop down to -5σ. This is because the number of background events is very low in some regions, resulting in gaps in the $M_{\gamma\gamma}$ distribution. Since the signal pdf is very narrow, the signal yield is set to very low values in the fitting process to fill the gap. This causes the observed outliers.

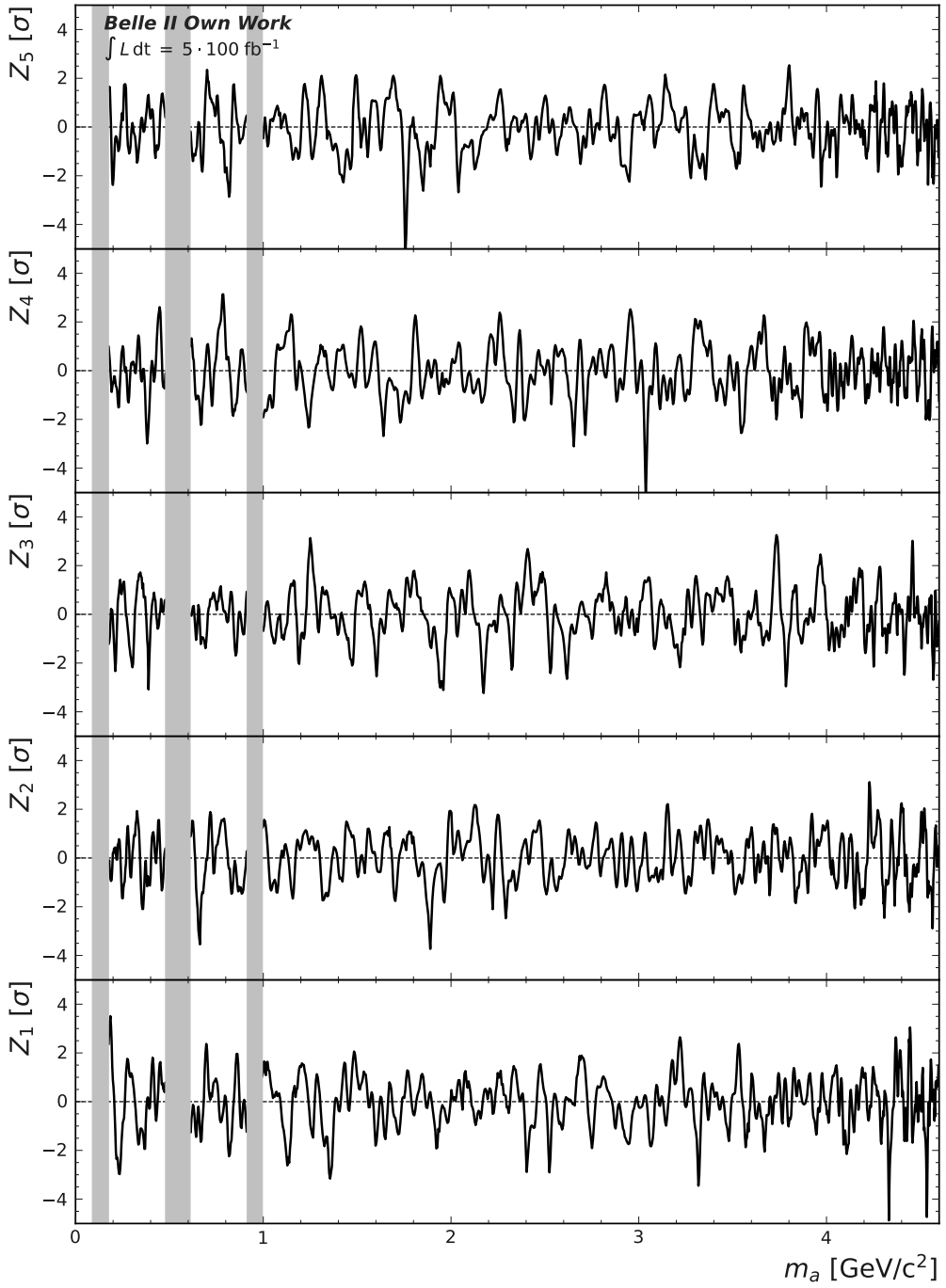

Figure C.1.: Significance of five different background MC samples corresponding to $100\,\mathrm{fb}^{-1}$ each as a function of m_a. Z_i is the significance of the i-th MC sample. The black dashed lines are aligned to a significance of 0σ. The gray vertical bands indicate the exclusion ranges of this analysis.

Bibliography

[1] G. Schott, "Hypothesis Testing", in *Data Analysis in High Energy Physics*, ch. 3, pp. 75–105. Wiley-VCH, 2013.

[2] F. Giacchino, "A light dark matter portal: The axion-like particle", *Frascati Phys. Ser.* **69** (Jun, 2019) 206–211. http://padme.lnf.infn.it/wp-content/uploads/sites/37/2019/10/frascatiphys_FGiacchino.pdf.

[3] E. Izaguirre, T. Lin, and B. Shuve, "Searching for Axionlike Particles in Flavor-Changing Neutral Current Processes", *Phys. Rev. Lett.* **118** no. 11, (Mar, 2017) 111802, arXiv:1611.09355 [hep-ph].

[4] K. Akai, K. Furukawa, and H. Koiso, "SuperKEKB Collider", *Nuclear Instruments and Methods in Physics Research Section A: Accelerators, Spectrometers, Detectors and Associated Equipment* **907** (Nov, 2018) 188–199, arXiv:1809.01958 [physics.acc-ph].

[5] **Particle Data Group**, P.A. Zyla et al., "Review of Particle Physics", *PTEP* **2020** no. 8, (Aug., 2020) 083C01.

[6] **BaBar Collaboration**, J. P. Lees et al., "Search for an Axion-Like Particle in B Meson Decays", arXiv:2111.01800 [hep-ex].

[7] R. D. Peccei and H. R. Quinn, "CP Conservation in the Presence of Pseudoparticles", *Phys. Rev. Lett.* **38** (Jun, 1977) 1440–1443.

[8] R. D. Peccei and H. R. Quinn, "Constraints imposed by CP conservation in the presence of pseudoparticles", *Phys. Rev. D* **16** (Sep, 1977) 1791–1797.

[9] S. Weinberg, "A New Light Boson?", *Phys. Rev. Lett.* **40** (Jan, 1978) 223–226.

[10] F. Wilczek, "Problem of Strong P and T Invariance in the Presence of Instantons", *Phys. Rev. Lett.* **40** (Jan, 1978) 279–282.

[11] B. Yoon, T. Bhattacharya, and R. Gupta, "Neutron Electric Dipole Moment on the Lattice", *EPJ Web of Conferences* **175** (2018) 01014, arXiv:1712.08557 [hep-lat].

[12] M. Gorghetto and G. Villadoro, "Topological Susceptibility and QCD Axion Mass: QED and NNLO corrections", *JHEP* **03** (Mar, 2019) 033, arXiv:1812.01008 [hep-ph].

[13] G. Alonso-Álvarez, M. B. Gavela, and P. Quilez, "Axion couplings to electroweak gauge bosons", *The European Physical Journal C* **79** no. 3, (Mar, 2019) , arXiv:1811.05466 [hep-ph].

[14] M. B. Gavela, R. Houtz, P. Quilez, R. Del Rey, and O. Sumensari, "Flavor constraints on electroweak ALP couplings", *The European Physical Journal C* **79** no. 5, (Apr, 2019) 369, arXiv:1901.02031 [hep-ph].

[15] P. Arias, D. Cadamuro, M. Goodsell, J. Jaeckel, J. Redondo, and A. Ringwald, "WISPy Cold Dark Matter", *JCAP* **06** (Jun, 2012) 013, arXiv:1201.5902 [hep-ph].

[16] M. A. Buen-Abad, J. Fan, M. Reece, and C. Sun, "Challenges for an axion explanation of the muon $g-2$ measurement", *Journal of High Energy Physics* **2021** no. 9, (Sep, 2021) , arXiv:2104.03267 [hep-ph].

[17] K. Lingel, T. Skwarnicki, and J. G. Smith, "Penguin decays of B mesons", *Annual Review of Nuclear and Particle Science* **48** no. 1, (Dec, 1998) 253–306, arXiv:hep-ex/9804015.

[18] **Belle II Collaboration**, E. Kou et al., "The Belle II Physics Book", *PTEP* **2019** no. 12, (Dec, 2019) 123C01, arXiv:1808.10567 [hep-ex].

[19] **Belle II Collaboration**, T. Abe et al., "Belle II Technical Design Report", arXiv:1011.0352 [physics.ins-det].

[20] Christian Pulvermacher, *dE/dx Particle Identification and Pixel Detector Data Reduction for the Belle II Experiment*. PhD thesis, Karlsruhe Institute of Technology (KIT), Karlsruhe, 2012. https://publish.etp.kit.edu/record/20770.

[21] **Belle II Framework Software Group**, T. Kuhr, C. Pulvermacher, M. Ritter, T. Hauth, and N. Braun, "The Belle II Core Software", *Computing and Software for Big Science* **3** no. 1, (Nov, 2018) 1, arXiv:1809.04299 [physics.comp-ph].

[22] R. Brun and F. Rademakers, "ROOT — An object oriented data analysis framework", *Nuclear Instruments and Methods in Physics Research Section A: Accelerators, Spectrometers, Detectors and Associated Equipment* **389** no. 1, (1997) 81–86. https://www.sciencedirect.com/science/article/pii/S016890029700048X. New Computing Techniques in Physics Research V.

[23] **Geant4 Collaboration**, S. Agostinelli et al., "Geant4 - a simulation toolkit", *Nuclear Instruments and Methods in Physics Research Section A: Accelerators, Spectrometers, Detectors and Associated Equipment* **506** no. 3, (Jul, 2003) 250–303. https://www.sciencedirect.com/science/article/pii/S0168900203013688.

[24] A. Ryd, D. Lange, N. Kuznetsova, S. Versille, M. Rotondo, D. P. Kirkby, F. K. Wuerthwein, and A. Ishikawa, "EvtGen: A Monte Carlo Generator for B-Physics",. https://evtgen.hepforge.org/doc/EvtGenGuide.pdf.

[25] **BaBar Collaboration**, D. Boutigny et al., *The BABAR physics book: Physics at an asymmetric B factory*. Okt, 1998. https://www.osti.gov/biblio/979931.

[26] M. Milesi, "Particle identification at Belle II with the Electromagnetic Calorimeter (ECL)", Presented for the Belle II StarterKit Workshop, Jan, 2020. https://indico.belle2.org/event/1307/sessions/378/attachments/3070/5670/mmilesi_ECLPid_B2SKW_2020.pdf. [Online; accessed 15.03.2022].

[27] V. Aulchenko, A. Bobrov, T. Ferber, A. Kuzmin, K. Miyabayshi, G. de Nardo, V. Shebalin, A. Sibidanov, Yu. Usov, and V. Zhulanov, "Time and energy reconstruction at

the electromagnetic calorimeter of the Belle-II detector", *Journal of Instrumentation* **12** no. 08, (Aug, 2017) C08001. https://doi.org/10.1088/1748-0221/12/08/c08001.

[28] Valerio Bertacchi et al., "Track finding at Belle II", *Computer Physics Communications* **259** (Feb, 2021) 107610, arXiv:2003.12466.

[29] J. Eschle, A. Puig Navarro, R. Silva Coutinho, and N. Serra, "zfit: Scalable pythonic fitting", *SoftwareX* **11** (2020) 100508, arXiv:1910.13429 [physics.data-an].

[30] J.-F. Krohn et al., "Global decay chain vertex fitting at Belle II", *Nuclear Instruments and Methods in Physics Research Section A: Accelerators, Spectrometers, Detectors and Associated Equipment* **976** (2020) 164269. https://www.sciencedirect.com/science/article/pii/S0168900220306653.

[31] A. J. Bevan et al., "The Physics of the B Factories", *The European Physical Journal C* **74** no. 11, (Nov, 2014) . http://dx.doi.org/10.1140/epjc/s10052-014-3026-9.

[32] M. Röhrken, *Time-Dependent CP Violation Measurements in Neutral B Meson to Double-Charm Decays at the Japanese Belle Experiment*. PhD thesis, Karlsruhe Institute of Technology (KIT), 2012. https://publish.etp.kit.edu/record/20864.

[33] G. Punzi, "Sensitivity of searches for new signals and its optimization", *eConf* **C030908** (Dec, 2003) MODT002, arXiv:physics/0308063.

[34] G. Cowan, *Statistical Data Analysis*. Oxford University Press, New York, 1998.

[35] F. James, *The Interpretation of Errors*, Jun, 2004. http://lmu.web.psi.ch/docu/manuals/software_manuals/minuit2/mnerror.pdf.

[36] J. Bennett, "Belle II Luminosity", Oct, 2019. https://confluence.desy.de/display/BI/Belle+II+Luminosity. [Online; accessed 10.03.2022].

[37] R. Andrae, T. Schulze-Hartung, and P. Melchior, "Dos and don'ts of reduced chi-squared", arXiv:1012.3754 [astro-ph.IM].

[38] M. Paterno, "Calculating efficiencies and their uncertainties", tech. rep., Fermilab, Dec, 2004. https://www.osti.gov/biblio/15017262.

[39] E. Gross and O. Vitells, "Trial factors for the look elsewhere effect in high energy physics", *The European Physical Journal C* **70** no. 1–2, (Oct, 2010) 525–530. http://dx.doi.org/10.1140/epjc/s10052-010-1470-8.

[40] G. Cowan, "The Look Elsewhere Effect", Presented for the ODSL Journal Club, Jun, 2021. http://www.pp.rhul.ac.uk/~cowan/stat/cowan_lee_25jun21.pdf. [Online; accessed 12.03.2022].

[41] G. Cowan, K. Cranmer, E. Gross, and O. Vitells, "Asymptotic formulae for likelihood-based tests of new physics", *The European Physical Journal C* **71** (2011) 1554, arXiv:1007.1727 [physics.data-an]. [Erratum: Eur.Phys.J.C 73, 2501 (2013)].